Recessive but damaging alleles of muscle-specific ribosomal protein gene *RPL3L* drive neonatal dilated cardiomyopathy

Michael R. Murphy[1,2#], Mythily Ganapathi[3], Teresa M. Lee[4], Joshua M. Fisher[4], Megha V. Patel[5,6], Parul Jayakar[7], Amanda Buchanan[8], Rajesh K. Soni[9], Yue Yin[1,2,10], Feiyue Yang[1,2], Muredach P. Reilly[1], Wendy K. Chung[11], & Xuebing Wu[1,2,#]

[1]Division of Cardiology, Department of Medicine, Columbia University Irving Medical Center, New York, NY 10032, USA

[2]Department of Systems Biology, Columbia University Irving Medical Center, New York, NY 10032, USA

[3]Department of Pathology and Cell Biology, Columbia University Irving Medical Center, New York, NY 10032, USA

[4]Department of Pediatrics, Columbia University Medical Center Irving Medical Center, New York, NY 10032, USA

[5]Department of Pediatrics, Nicklaus Children's Hospital, Miami, FL 33155, USA

[6]Current: Children's Wisconsin, Medical College of Wisconsin, Milwaukee, WI 53226, USA

[7]Division of Genetics and Metabolism, Nicklaus Children's Hospital, Miami, FL 33155, USA

[8]Illumina Inc., San Diego, CA, USA

[9]Proteomics and Macromolecular Crystallography Shared Resource, Herbert Irving Comprehensive Cancer Center, Columbia University, New York, NY 10032, USA

[10]Barnard College, Columbia University, New York, NY 10027, USA

[11]Department of Pediatrics, Boston Children's Hospital, Harvard Medical School, Boston, MA 02115, USA

[#]Correspondence to: mrm2267@cumc.columbia.edu (M.R.M); xuebing.wu@columbia.edu (X.W.)

Abstract

The heart employs a specialized ribosome in its muscle cells to translate genetic information into proteins, a fundamental adaptation with an elusive physiological role. Its significance is underscored by the discovery of neonatal patients suffering from often fatal heart failure caused by rare compound heterozygous variants in RPL3L, a muscle-specific ribosomal protein that replaces the ubiquitous RPL3 in cardiac ribosomes. *RPL3L*-linked heart failure represents the only known human disease arising from mutations in tissue-specific ribosomes, yet the underlying pathogenetic mechanisms remain poorly understood despite an increasing number of reported cases. While the autosomal recessive inheritance pattern suggests a loss-of-function mechanism, *Rpl3l*-knockout mice display only mild phenotypes, attributed to up-regulation of the ubiquitous Rpl3. Interestingly, living human knockouts of *RPL3L* have been identified. Here, we report two new cases of *RPL3L*-linked severe neonatal heart failure and uncover an unusual pathogenetic mechanism through integrated analyses of population genetic data, patient cardiac tissue, and isogenic cells expressing *RPL3L* variants. Our findings demonstrate that patient hearts lack sufficient RPL3 compensation. Moreover, contrary to a simple loss-of-function mechanism often associated with autosomal recessive diseases, *RPL3L*-linked disease is driven by a combination of gain-of-toxicity and loss-of-function. Most patients carry a recurrent toxic missense variant alongside a non-recurrent loss-of-function variant. The non-recurrent variants trigger partial compensation of *RPL3* similar to *Rpl3l*-knockout mice. In contrast, the recurrent missense variants exhibit increased affinity for the *RPL3/RPL3L* chaperone GRWD1 and 60S biogenesis factors, sequester 28S rRNA in the nucleus, disrupt ribosome biogenesis, and trigger severe cellular toxicity that extends beyond the loss of ribosomes. These findings elucidate the pathogenetic mechanisms underlying muscle-specific ribosome dysfunction in neonatal heart failure, providing critical insights for genetic screening and therapeutic development. Our findings also suggest that gain-of-toxicity mechanisms may be more widespread in autosomal recessive diseases, especially for those involving genes with paralogs.

Main

The heart is a remarkable organ, beating continuously throughout a human lifetime with a minimal need to replenish its muscle cells (cardiomyocytes)[1]. This extraordinary durability is attributed to many unique adaptations in cardiomyocytes. One of the most fundamental yet least understood adaptations is that cardiomyocytes use a specialized ribosome to decode genetic information and synthesize proteins[2-4]. Although ribosomes in all cells use the same genetic code, the composition of the ribosome itself—a delicate molecular machine comprising 80 ribosomal proteins and 4 ribosomal RNAs (rRNAs)—can differ across cell types[5-11]. The most striking variation occurs in cardiomyocytes. During vertebrate heart development, the ubiquitous core ribosomal protein L3 (RPL3), which makes the closest contact of any protein to the ribosome's RNA-based catalytic center[12], is gradually replaced by its paralog, RPL3-like (RPL3L)[2, 13]. RPL3L shares 74% amino acid identity with RPL3[2, 3] and eventually becomes the dominant form in adult human left ventricular cardiomyocytes (95%)[14], to a lesser extent in skeletal muscle (60%), and barely detectable in non-muscle cells[15]. Interestingly, this switch is reversed during adult muscle growth (hypertrophy) following injury or atrophy[3, 16, 17]. The physiological role of this highly conserved and tightly regulated ribosomal switching remains poorly understood, highlighting a crucial gap in our understanding of cardiac biology at the most fundamental level.

The essential role of RPL3L and the specialized ribosome in the heart is underscored by an increasing number of severe neonatal dilated cardiomyopathy (DCM) cases linked to biallelic variants in *RPL3L*[18-23]. This has been designated as a new DCM subtype, Dilated Cardiomyopathy-2D (CMD2D, OMIM# 619371). It stands out as most known DCM genes encode proteins associated with the sarcomere[24-26], the contractile unit of the muscle. *RPL3L*-linked DCM was the first—and remains the only—known human disease caused by mutations in tissue-specific ribosomes. Among seven independent affected families, individuals with mutations in both *RPL3L* alleles consistently develop severe DCM, often resulting in fatal heart failure[18-23]. In contrast, heterozygous parents and siblings carrying a single mutant allele remain unaffected with the early onset CMD2D. While the autosomal recessive inheritance pattern suggests a loss-of-function of these alleles and RPL3L deficiency as the likely cause of DCM, *Rpl3l* knockout (KO) mice generated by multiple labs display only mild cardiac dysfunction[4, 16, 27, 28]. This is unexpected given the 96% homology between human and mouse RPL3L proteins and that the highly regulated RPL3-RPL3L switch is also conserved in mice[16].

The discrepancy between early onset fatal disease in humans and mild phenotypes in mice suggests either species-specific differences in heart biology or that the DCM-causing autosomal recessive *RPL3L* mutations have effects beyond simple loss-of-function, rendering them unsuitable for modeling with KO mice. While rarely reported, autosomal recessive mutations can cause disease via toxic gain-of-function[29]. Notably, in all *Rpl3l* KO mouse models, regardless how they were generated—whether through a frameshifting deletion of the entire exon 2[4], short frameshifting deletions in exon 5[16, 27], or poly(A) insertion in exon 1[28]—there is a consistent up-regulation of the ubiquitous paralog Rpl3. This compensatory increase in Rpl3 likely explains the absence of a severe cardiac phenotype in mice, as Rpl3 is expected to largely fulfill the functional role of Rpl3l. The molecular mechanism underlying the *Rpl3* compensation remains unclear.

99 Whether a lack of *RPL3* compensation in human underlie the severe DCM symptoms remains
100 unexplored. A deeper understanding of the pathogenetic mechanism of *RPL3L*-linked DCM,
101 including whether *RPL3* compensation occurs and how to activate the compensation, may inform
102 future management and the development of new therapeutics for these patients.

103 To date, more than ten *RPL3L* mutations have been associated with neonatal DCM[18-23], with new
104 variants identified in every affected family. The relative importance of these variants in disease
105 remains unclear, as no functional characterizations have been performed. Here, we report two
106 new cases of *RPL3L*-linked DCM that along with previous cases highlight the existence of two
107 hotspot variants, suggestive of allele-specific pathogenetic mechanisms. We systematically
108 validated these hypotheses using patient tissue and isogenic cell lines expressing various *RPL3L*
109 variants.

110 Hotspot G27D and D308N/V are potential driver mutations

111 We identified two additional unrelated cases of *RPL3L*-associated early onset CMD2D, increasing
112 the total number of affected families to nine (Supplemental Information). Similar to previously
113 reported cases[18-23], both of the two families are associated with compound heterozygous variants,
114 i.e., each affected individual carry two different variants on separate alleles.
115
116 Interestingly, both cases share D308N as one of the variants: D308N/R58Q and
117 D308N/T340Nfs*25 (c.1080dup), respectively. A review of all the cases of *RPL3L*-linked DCM
118 reveals that while mutations are distributed across nearly the entire RPL3L protein (**Fig. 1a-b**), two
119 notable hotspots emerge: glycine at position 27 (G27) and aspartic acid at position 308 (D308) (**Fig.
120 1a**). Specifically, the G27D mutation is present in three of the nine families, while mutations at
121 D308 (D308N and D308V) appear in four additional families. These nine families originate from six
122 different countries and are presumed to be unrelated. For example, the three families carrying the
123 G27D variant are located in the United States, Spain, and China.
124
125 Although all *RPL3L* variants implicated in DCM are exceedingly rare in the general population ($<10^{-}$
126 ^{4}, gnomAD[30]), the two hotspot variants (G27D and D308N/V) have even lower allele frequencies
127 ($<10^{-5}$) compared to other DCM-linked *RPL3L* variants (**Fig. 1c**), indicating stronger negative
128 selection and greater deleterious effects. Indeed, G27D and D308N/V are predicted to be highly
129 pathogenic by AlphaMissense[31], a state-of-the-art deep learning model that builds on the protein
130 structure prediction tool AlphaFold2[32]. The low allele frequencies of these mutations in the
131 general population further argue against the hypothesis that the recurrence of G27D and D308N/V
132 in patients is due to increased mutability of the DNA bases. The recurrent occurrence of these
133 ultra-rare missense mutations in a substantial proportion of DCM families strongly challenges a
134 loss-of-function mechanism, particularly given the high conservation of much of the protein and
135 the fact that neither G27 nor D308 is among the residues known to be critical for RPL3/RPL3L's
136 role in the ribosome. Together, G27D and D308N/V account for 78% (7/9) of *RPL3L*-linked DCM
137 families, positioning them as the primary driver mutations in the disease.

138 Notably, the ten missense variants can be divided into two groups when considering allele
139 frequency and pathogenicity predicted by AlphaMissense (**Fig. 1c**). In addition to the hotspot
140 mutations G27D and D308N/V, the high-pathogenicity group includes the V231F mutation,
141 another extremely rare (~10^{-6}) mutation in the population and predicted to be highly pathogenic
142 by AlphaMissense. It is possible that with more cases to be discovered, V231F may also be found
143 to be a hotspot mutation similar to G27D and D308N/V in the same group. Variants in the low-
144 pathogenicity group are more frequent (still very rare, 10^{-5} to 10^{-4}) and predicted to be less
145 pathogenic (**Fig. 1c**). Interestingly, with the exception of the homozygous R116H mutation
146 (identified in a consanguineous population[21]), each affected individual carries one mutation from
147 the high-pathogenicity group and another mutation from the low-pathogenicity group (linked by
148 dashed lines).

149 Consistent with the absence of a severe cardiac phenotype in *Rpl3l* KO mice, live human knockouts
150 of *RPL3L* have been identified in large-scale genetic studies, including gnomAD[30], All of Us[33], and
151 UK Biobank[34] (**Fig. 1d**). One individual carries a premature stop codon at arginine 226 in both
152 alleles (R226X), truncating nearly half of the protein (full-length RPL3L is 407 amino acids), a
153 mutation almost certainly resulting in loss-of-function. Additionally, a total of 17 individuals are
154 homozygous for a splice donor variant previously shown to cause exon 9 deletion, which removes
155 a highly conserved 40-amino-acid region in RPL3L[35]. Although this splice donor variant is
156 associated with an increased risk of atrial fibrillation (OR: 1.50) in a genome-wide association
157 study[35], homozygous individuals carrying this variant appear to be alive and do not exhibit early-
158 onset severe DCM. There are also nine putative knockout humans in the Regeneron Genetics
159 Center Million Exome (RGC-ME) database[36] although detailed information about these variants is
160 not available. The lack of severe cardiac dysfunction in both putative *RPL3L* KO humans and *Rpl3l*
161 KO mice strongly suggests that the missense *RPL3L* mutations identified in DCM patients are not
162 simply loss-of-function variants.

163 In summary, genetic evidence indicates that hotspot missense mutations at G27 and D308 in
164 *RPL3L* likely cause DCM through a mechanism other than loss-of-function, despite an autosomal
165 recessive inheritance pattern.

166 Ribosome defects in explanted patient hearts

167 To investigate the pathogenic mechanisms of *RPL3L* mutations in DCM, we initially focused on a
168 patient carrying the hotspot D308N allele and the T189M missense allele. This patient, diagnosed
169 and treated at our center, underwent heart transplantation and is alive to date[18]. Using explanted
170 heart ventricular tissues, we extracted total RNA to perform RNA-seq and compared the results to
171 age-matched control healthy heart ventricular tissues.

172 Unexpectedly, we observed an abnormality when the total RNA was subjected to Bioanalyzer
173 electrophoresis for quality check (**Fig. 2a**). Specifically, there is a drastic reduction in the 28S rRNA
174 peak relative to the 18S peak. The 28S rRNA is the scaffold of the 60S large subunit of the ribosome.
175 RPL3L (and the paralog RPL3) is a core component of the 60S subunit and plays a vital role in 60S
176 ribosome biogenesis via its interaction with the 28S rRNA[37]. The loss of 28S rRNA indicates a defect

177 in 60S ribosome biogenesis in patient cells, presumably due to the D308N/T189M mutations in
178 *RPL3L*.

179 The RNA-seq data revealed widespread alterations in gene expression, including 1,639 significantly
180 up-regulated genes and 2,361 significantly down-regulated genes (**Fig. 2b**). Pathway analyses
181 confirmed up-regulation of gene signatures associated with systolic heart failure and apoptosis,
182 and interestingly, a massive up-regulation of genes associated with fetal cardiac myeloid cells,
183 consistent with increased inflammation in failing hearts[38] (**Fig. 2c**).

184 In line with impaired ribosome biogenesis, many ribosomal protein genes are differentially
185 expressed, with more down-regulated than up-regulated (**Fig. 2b**). *RPL3L* is down-regulated by
186 approximately two-fold, although not significantly (adjusted P = 0.6). Both D308N and T189M
187 alleles are expressed at a similar level as indicated by sequencing read coverage (**Fig. 2d**).

188 Surprisingly, unlike the robust increase of *Rpl3* mRNA and protein in *Rpl3l* KO mice, there was no
189 compensatory up-regulation of *RPL3* mRNA in the patient's heart tissue (**Fig. 2b**). Instead, *RPL3* is
190 slightly down-regulated (by 24%, adjusted P=0.66) like many other ribosomal protein genes.

191 To confirm the lack of *RPL3* compensation in the DCM heart tissue, we also examined protein
192 expression using mass spectrometry. Indeed, when normalized to the total abundance of 40S
193 ribosomal proteins, there is a significant decrease in RPL3 abundance with no change in RPL3L (**Fig.**
194 **2e**). Consistent with a 60S biogenesis defect, there is a mild but significant decrease in total 60S
195 ribosomal protein level relative to that of the 40S. Similar to the RNA-seq data (**Fig. 2d**), the D308N
196 allele is expressed at a comparable level as the T189M allele (**Fig. 2f**).

197 In the absence of compensatory RPL3 up-regulation, there will be a shortage of functional 60S
198 ribosomes in patient cells, as neither functional RPL3L nor RPL3 is present. Given the critical role
199 of ribosomes in cellular function, the loss of functional ribosomes likely contributes to
200 cardiomyocyte death and the progression of DCM. While caveats remain (see Discussion), the lack
201 of RPL3 compensation observed in human DCM patients underscores a critical divergence from
202 the *Rpl3l* KO mouse model and suggests that at least one of the two missense *RPL3L* variants
203 (D308N and T189M) are unlikely to function as simple loss-of-function alleles.

204 In summary, analysis of explanted heart tissues from DCM patients demonstrates a defect in 60S
205 ribosome biogenesis and a lack of RPL3 compensation. These defects likely contribute to the loss
206 of functional ribosomes, cardiomyocyte death, and the development of heart failure in *RPL3L*-
207 linked DCM.

208 Hotspot variants gain toxic function to drive ribosome biogenesis defects and cellular toxicity

209 It remains unclear whether the ribosome biogenesis defect observed in explanted patient tissue
210 is caused by the hotspot D308N mutation or the accompanying T189M allele. Both alleles are
211 expressed at comparable levels with no significant allele imbalance (**Fig. 2d** and **Fig. 2F**).

212 To determine the individual impact of these alleles, we generated isogenic cell lines expressing
213 various RPL3L variants in the absence of RPL3 (**Fig. 3a**). These cell lines were derived from human
214 AC16 cells, ventricular cardiomyocyte-like cells commonly used to study cardiac gene expression
215 and function[39], including the regulation of ribosomes and translation in cardiac hypertrophy[40].
216 While AC16 cells do not fully recapitulate primary cardiomyocytes, our results described below
217 demonstrate their suitability for studying ribosome-related processes. Of note, *RPL3L* is not
218 expressed in iPSC-derived cardiomyocytes (iPSC-CMs) (**Extended Data Fig. 1**), consistent with the
219 notion that iPSC-CMs resemble immature fetal cardiomyocytes[41, 42], while *RPL3L* expression is
220 restricted to mature cardiomyocytes.

221 Wild-type AC16 cells naturally express only *RPL3*, not *RPL3L*. To switch to *RPL3L* variants, we first
222 introduced a doxycycline (dox)-inducible shRNA targeting *RPL3* to deplete RPL3 in an inducible
223 manner. This cell line (shRPL3-only) serves as a critical baseline control for the cellular defect and
224 toxicity caused by the loss-of-function of ribosomal proteins. Using shRPL3-only cells, we further
225 integrated a second dox-inducible transgene expressing HA-tagged *RPL3L*, either the wild type or
226 variants (**Fig. 3a**). In addition to DCM-linked *RPL3L* variants, we also included a common SNP
227 (rs34265469) predicted to result in a benign missense variant (P291L). This SNP is the most
228 common missense variant in *RPL3L*, with an allele frequency of 4.26% (TOPMed) and is
229 homozygous in at least 715 living individuals. This isogenic system enabled allele-specific switching
230 from *RPL3* to *RPL3L* at physiological level upon dox treatment (**Fig. 3b-c**).

231 Using these isogenic cell lines, we found that the loss of the 28S rRNA observed in the explanted
232 patient heart tissue (**Fig. 2a**) was faithfully recapitulated in cells expressing the D308N allele, but
233 not in those expressing the T189M allele (**Fig. 3d**). Notably, the loss of 28S rRNA in D308N cells is
234 much stronger than that of the shRPL3-only cells (**Fig. 3d**). Given that the only difference between
235 these two cell lines is the expression of the D308N variant, the stronger defect indicates toxic gain-
236 of-function of the D308N variant. Additionally, the weaker effect in the shRPL3-only cells suggests
237 that ribosome loss alone is insufficient to fully account for the defects observed in patients (**Fig.**
238 **2a**).

239 Consistent with 60S ribosomal subunit biogenesis defects, sucrose gradient sedimentation
240 revealed a dramatic reduction in 60S but not 40S ribosomal subunits in D308N-expressing cells
241 compared to WT, SNP, or T189M cells (**Fig. 3e**). Accordingly, monosomes (80S) and translating
242 polysomes (poly-ribosomes), both of which contain 60S, are also depleted in D308N-expressing
243 cells (**Fig. 3e**). Notably, the loss of polysomes in D308N-expressing cells is comparable to cells not
244 expressing any *RPL3L* variant (shRPL3-only) (**Fig. 3e**), suggesting the D308N variant of RPL3L almost
245 completely blocks ribosome biogenesis.

246 In line with a severe loss of ribosomes, D308N-expressing cells exhibited a severe growth defect
247 (**Fig. 3f**, note that the y-axis is on a logarithmic scale). Expressing D308N for 10 days led to a 40-
248 fold reduction in cell counts (compared to RPL3L-WT cells, **Fig. 3f**, green vs. red). Interestingly,
249 cells expressing the D308N variant exhibit a 6.4-fold greater growth defect compared to cells
250 lacking RPL3L expression (shRPL3-only) (green vs. blue, **Fig. 3f**), again suggesting toxic gain-of-
251 function. Of note, the control cell line expressing RPL3 (shScramble) grew faster than cells

252 expressing wild type RPL3L (RPL3L-WT), mirroring a previous mouse study showing that Rpl3l
253 expression is associated with reduced protein synthesis and slower muscle cell growth[3].
254 Interestingly, cells expressing the T189M variant of *RPL3L* grew faster than cells expressing the
255 wild type *RPL3L*, which may be attributed to a higher expression of *RPL3* in this cell line (**Fig. 3b**,
256 also see below the discussion on *RPL3* compensation). The lack of deleterious effects associated
257 with the T189M variant aligns with its low pathogenicity prediction by AlphaMissense (**Fig. 1c**) and
258 is further supported by the presence of a living homozygous T189M individual in the population
259 genotyped in TOPMed. Taken together, these results indicate that the D308N variant is a toxic
260 gain-of-function variant and the primary driver of the disease in the patient carrying D308N and
261 T189M.

262 Next, we investigated the other hotspot variant G27D, together with the R161W allele found in
263 the same affected individual[18]. Similar to the D308N variant, cells expressing the G27D variant
264 grew substantially slower than those expressing the wild-type *RPL3L* allele (33-fold fewer cells by
265 day 10, **Extended Data Fig. 2a**), whereas cells expressing the R161W variant grew slightly faster
266 than cells expressing the WT RPL3L, similar to T189M. Consistent with a growth defect, G27D but
267 not R161W-expressing cells are depleted of 60S and 80S ribosomes as well as polysomes
268 (**Extended Data Fig. 2b**). These findings confirm that the hotspot variants G27D and D308N, but
269 not their co-inherited non-hotspot variants T189M and R161W, are responsible for ribosome
270 biogenesis defects and cellular toxicity.

271 ## Hotspot variants mislocalize and alter interactions with ribosome biogenesis factors

272 To further explore the molecular basis of the toxic gain-of-function of the hotspot variants, we
273 examined the subcellular localization of RPL3L variants using fluorescence imaging of the HA tag.
274 In contrast to the predominantly cytoplasmic localization of the wild-type RPL3L and the common
275 SNP variant expected from a ribosomal protein, the hotspot variants D308N and G27D both
276 exhibited nearly exclusive nuclear localization (**Fig. 4a**, green, quantified in **Fig. 4b**). Given the role
277 of RPL3/RPL3L in 60S ribosome biogenesis, this mislocalization of the hotspot variants likely disrupt
278 60S ribosome assembly. Supporting this, fluorescent probes for 28S rRNA revealed a significant
279 decrease in cytoplasmic 28S rRNA levels in D308N or G27D-expressing cells relative to the nucleus
280 (**Fig. 4a**, red, quantified in **Fig. 4c**). Notably, this 28S rRNA localization defect was not observed in
281 cells not expressing any RPL3L variant (shRPL3-only), consistent with a toxic gain-of-function of
282 both hotspot variants.

283 To gain biochemical insights into the toxicity associated with the hotspot variants, we profiled the
284 interactomes of RPL3L variants by using immunoprecipitation against HA-tag followed by mass
285 spectrometry in triplicates. Given the exclusive nuclear localization of the hotspot variants, we
286 used nuclear lysate as input for all samples. Interestingly, principal component analysis (PCA) of
287 the proteomics data separates the two hotspot variants from the rest in the first principal
288 component (PC1), suggesting dramatic rewiring of the interactome for hotspot variants (**Fig. 4d**).
289 The second principal component (PC2) separates the three nuclear variants (G27D, D308N, and
290 R161W) from the two cytoplasmic variants (T189M and WT). Interestingly, the top two proteins
291 driving the separation of hotspot variants from other variants both exhibit increased affinity for

292 the hotspot variants, supporting the concept of toxic gain-of-function effects (**Fig. 4e**). These two
293 proteins, GRWD1 and C7ORF50, although less studied in humans, have yeast homologs (Rrb1 and
294 Rbp95, respectively) that directly interact with yeast Rpl3 during 60S ribosome biogenesis. GRWD1
295 serves as the dedicated chaperone for RPL3 (and likely RPL3L as well), binding RPL3 co-
296 translationally to prevent its aggregation and degradation, ensuring its proper delivery to the
297 assembly site on nucleolar pre-60S particles[43-45]. The other protein, C7ORF50, interacts with RPL3
298 both genetically and physically, binding adjacent to RPL3 on the 28S rRNA during early pre-60S
299 ribosome biogenesis[46-48]. Several other 60S biogenesis factors, including RRP15[49], EBNA1BP2[50],
300 DDX24[51], NOP56[47], and MRTO4[52] also exhibited enrichment in the nuclear pulldown of RPL3L
301 variants (**Extended Data Fig. 3**). The sequestration of these essential 60S ribosome biogenesis
302 factors by hotspot variants likely underlies the 60S biogenesis defect and contributes to the toxic
303 gain-of-function effects associated with these variants.
304
305 In summary, our subcellular localization analysis and nuclear protein interactome profiling using
306 isogenic cell lines reveal that the hotspot variants D308N and G27D mislocalize to the nucleus,
307 leading to nuclear retention of 28S rRNA. This toxic effect is likely driven by their enhanced binding
308 to the dedicated RPL3/RPL3L chaperone GRWD1 and 60S ribosome biogenesis factors, including
309 C7ORF50.

310 ## Non-hotspot variants drive post-transcriptional *RPL3* compensatory up-regulation

311 Intriguingly, the non-hotspot R161W allele, identified in the same affected individual as the
312 hotspot G27D, also mislocalizes to the nucleus (**Fig. 4a-b**). However, unlike the hotspot variants
313 and consistent with its lower predicted pathogenicity (**Fig. 1c**), R161W does not cause nuclear
314 sequestration of 28S rRNA (**Fig. 5a/c**), nor does it lead to a ribosome biogenesis defect (**Extended**
315 **Data Fig. 2a**) or cell toxicity (**Extended Data Fig. 2b**). Western blot analysis of the polysome
316 fractions confirmed the absence of R161W from these ribosomes (**Extended Data Fig. 4**).

317 To investigate how ribosomes can still function in the absence of cytoplasmic RPL3L, we examined
318 the expression of RPL3, which was expected to be silenced by an shRNA induced alongside the
319 R161W allele upon dox treatment (**Fig. 3a**). Unexpectedly, while *RPL3* remained silenced in cells
320 expressing most *RPL3L* alleles, its expression was almost fully restored in cells expressing the
321 R161W allele, and to a lesser extent in those expressing the T189M allele, at both the mRNA (**Fig.**
322 **5a**) and protein (**Fig. 5b**) levels. Importantly, there was no significant change in the expression of
323 the *RPL3*-targeting shRNA (**Extended Data Fig. 5**), ruling out the possibility that *RPL3* recovery was
324 due to loss of shRNA-mediated knockdown in cells expressing R161W or T189M. These results
325 suggest that, similar to *Rpl3l*-KO mice, the expression of the non-hotspot *RPL3L* alleles R161W and
326 T189M leads to compensatory up-regulation of *RPL3*, suggesting that these alleles are functionally
327 equivalent to a knockout of *RPL3L*. Supporting a model in which compound heterozygotes carry a
328 toxic hotspot variant alongside a loss-of-function variant, frameshifting variants were identified in
329 three of the seven families with hotspot variants (**Fig. 1a**).

330 To elucidate the mechanism behind this *RPL3* compensation, we first examined the transcriptional
331 activity at the *RPL3* promoter using chromatin immunoprecipitation (ChIP) against RNA

332 polymerase II (Pol II). No significant differences in transcriptional activity were observed between
333 cells expressing G27D and R161W (**Fig. 5c**). Additionally, qPCR measurements of nascent
334 transcription from intronic RNA showed no significant differences (**Extended Data Fig. 6**), ruling
335 out transcriptional up-regulation as the mechanism of *RPL3* compensation.

336 We then assessed the stability of *RPL3* mRNA by inhibiting global transcription with the RNA Pol II
337 inhibitor α-amanitin and measuring the decay of *RPL3* mRNA over time. Compared to cells
338 expressing the G27D allele, *RPL3* mRNA was significantly more stable in cells expressing the
339 R161W allele (**Fig. 5d**, $P < 0.05$). Consistent with a post-transcriptional mechanism, the increase in
340 steady-state *RPL3* level was primarily due to increased cytoplasmic *RPL3*, with no significant
341 change in the nuclear fraction (**Fig. 5e**).

342 In summary, unlike the two hotspot alleles, G27D and D308N, which exhibit a gain-of-toxic
343 function, the non-hotspot alleles R161W and T189M resemble a knockout effect, promoting
344 compensatory upregulation of *RPL3* by stabilizing its mRNA.

345 Impaired protein synthesis in engineered compound heterozygous cells

346 *RPL3L*-linked DCM patients often carry a combination of a hotspot allele and a non-hotspot allele,
347 such as the D308N/T189M and G27D/R161W pairs we have characterized. In our analysis of
348 explanted heart tissue from patients carrying the D308N/T189M alleles, both alleles were
349 detected at the RNA (**Fig. 2d**) and protein levels (**Fig. 2f**). Given the opposing effects of the hotspot
350 and non-hotspot alleles on ribosome biogenesis and cell growth (**Fig. 3-5**), we sought to explore
351 the impact of these alleles when both are present in the same cell, as is common in most DCM
352 patients.

353 To address this, we introduced the G27D allele into cells expressing the R161W allele, creating a
354 model of compound heterozygous cells that mirror those found in DCM patients. We chose R161W
355 over T189M because R161W triggers a stronger compensatory up-regulation of *RPL3* (**Fig. 5a-b**).
356 Using a puromycin incorporation assay to measure nascent protein synthesis, we observed a
357 significant reduction in protein synthesis rates in the compound heterozygous cells compared to
358 those expressing R161W alone, though the rate was still higher than in cells expressing G27D alone
359 (**Fig. 6a-b**). This reduced protein synthesis rate aligns with the observed detrimental effects of
360 compound heterozygous *RPL3L* alleles in humans.

361 Interestingly, *RPL3* compensation remained unaffected in the compound heterozygous cells
362 compared to cells expressing R161W alone (**Fig. 6c**). This suggests that the compensatory up-
363 regulation of *RPL3* is not sufficient to overcome the toxic effects of the G27D allele.

364 Discussion

365 In this study, we reported two new cases of severe neonatal heart failure caused by mutations in
366 the muscle-specific ribosomal protein RPL3L and uncovered a complex mechanism by which these
367 mutations cause disease. Our study revealed a pattern hidden in the large number of variants
368 found in patients. Specifically, a small number of recurrent, toxic variants co-occur with likely loss-

369 of-function variants in each affected individual. Our study suggests an unexpected pathogenetic
370 mechanism—autosomal recessive mutations exerting gain-of-toxic function other than merely
371 loss-of-function effects—underlie the severe heart defects in humans and may also explain the
372 lack of phenotype in *Rpl3l* KO mice. Here we discuss the significance of our discovery as well as
373 questions remain to be addressed.

374 DCM is a leading cause of heart failure, with nearly half of all cases—and two-thirds of pediatric
375 cases—remaining of unknown etiology[24, 25, 53, 54]. This underscores the urgent need to identify and
376 understand novel pathogenic mechanisms to improve management and treatment. The advent of
377 accessible human exome sequencing and whole-genome sequencing has led to a renaissance in
378 the discovery of causal disease genes for DCM, including in pathways not previously known to have
379 specific cardiac function[55]. This itself has resulted in a lag between causal gene discovery and
380 research underlying disease mechanisms[56]. In the case of *RPL3L*, there has been no functional
381 studies to understand how mutations on the cardiac ribosome cause DCM. Here, we address this
382 gap by experimentally characterizing multiple *RPL3L* mutations, uncovering their impact on
383 ribosome biogenesis, protein synthesis, and cell viability.

384 Our findings suggest that rather than a simple loss-of-function mechanism, these autosomal
385 recessive missense mutations in *RPL3L* cause disease via a combination of gain-of-toxicity and loss-
386 of-function mechanism, supported by both genetic and biochemical evidence. Hotspot variants in
387 rare diseases are more commonly associated with toxic effects or even dominant-negative traits[57-
388 59]. Despite their rarity in the general population, missense mutations G27D and D308N/V occur in
389 seven out of nine unrelated DCM patient families. Mechanistically, hotspot variants of RPL3L
390 mislocalize to the nucleus and disrupt ribosome biogenesis when expressed in human cells,
391 recapitulating the 28S rRNA loss observed in explanted patient hearts carrying the same mutation.
392 Mislocalization of hotspot variants also caused 28S rRNA retention in the nucleus, a defect not
393 seen with RPL3 knockdown, indicating toxicity beyond loss-of-function. This toxic effect is likely
394 caused by enhanced binding to GRWD1 and other ribosome biogenesis factors. Ribosome
395 biogenesis defects result in the loss of global protein synthesis and reduced cell viability, again
396 beyond the simple loss of ribosomes. Future studies, especially *in vivo* studies will be needed to
397 elucidate how these molecular and cellular defects lead to organ level failure.

398 Autosomal recessive mutations in Mendelian disorders are typically considered loss-of-function
399 mutations[60]. Rarely do they cause disease via gain-of-toxicity or dominant-negative mechanisms.
400 The only prior example known is the A673V missense mutation in the β-amyloid (Aβ) precursor
401 protein (APP), associated with familial Alzheimer's disease[29]. In this case, the mutant allele in the
402 homozygous state enhances Aβ peptide production, promoting the formation of amyloid fibrils,
403 the primary trigger of Alzheimer's disease. In heterozygous individuals, however, the coexistence
404 of wild-type and mutant Aβ peptides inhibits amyloidogenesis relative to either mutant or wild-
405 type Aβ peptide alone. This inhibition is likely due to conformational incompatibility between the
406 wild-type and mutant Aβ peptides. For *RPL3L*-linked heart failure, there are several possibilities
407 for why heterozygous members of families carrying the recurrent and toxic variant (e.g., G27D and
408 D308N/V) have not developed severe disease. The presence of the wild type RPL3L protein will
409 likely reduce the toxicity and result in incomplete penetrance or much delayed onset of the disease.

410 One plausible mitigation mechanism is that these RPL3L hotspot variants form aggregates similar
411 to Aβ, with wild-type RPL3L in heterozygous cells preventing such aggregation and mitigating the
412 pathogenic effects.

413 Compensation by the paralog RPL3, triggered by RPL3L loss-of-function, likely explains why severe
414 disease arises only from a combined gain-of-toxicity and loss-of-function mechanism, rather than
415 loss-of-function alone. Genetic compensation by paralogs is well-documented, although the
416 underlying molecular mechanisms often remain unclear[61-63]. The increased expression of *Rpl3*
417 observed in *Rpl3l* KO mice has been proposed to explain the absence of severe cardiac phenotypes
418 in these animals, but the molecular basis of this compensation is not yet understood. In this study,
419 we demonstrate that non-hotspot missense mutations, such as R161W, also up-regulate *RPL3*
420 expression in human cells. This up-regulation occurs through stabilization of cytoplasmic *RPL3*
421 mRNA without transcriptional activation. However, the *RPL3* compensation induced by the R161W
422 variant does not fully counteract the toxic effects of the G27D variant when co-expressed in
423 human cells. These findings suggest that enhancing *RPL3* compensation alone may be insufficient
424 as a therapeutic strategy for patients carrying toxic *RPL3L* mutations.

425 We observed no significant *RPL3* compensation in failing hearts explanted from human DCM
426 patients with *RPL3L* mutations, in stark contrast to the robust up-regulation of *Rpl3* observed in
427 *Rpl3l* KO mice. This difference may help explain the discrepancy in disease manifestation between
428 humans and mice. However, our analysis has several limitations. The comparison was made
429 between DCM patient ventricular tissues and three age-matched healthy controls, which showed
430 considerable variation in *RPL3* expression. Moreover, these controls were from individuals without
431 cardiomyopathy or other cardiac conditions. Since the RPL3/RPL3L switch is known to be regulated
432 during muscle hypertrophy, it remains challenging to determine whether changes in *RPL3*
433 expression—or the lack thereof—are a cause or consequence of DCM. Future studies, including
434 mouse models carrying human-specific mutations, will be essential to confirm these findings and
435 further elucidate the underlying mechanisms.

436 In conclusion, our systematic genetic and functional analyses provide new insights into the
437 pathogenesis of heart failure caused by mutations in muscle-specific ribosomes, uncovering a
438 novel mechanism involving gain-of-toxic effects of recessive mutations. These findings lay the
439 groundwork for understanding other *RPL3L* variants and offer a foundation for developing
440 targeted therapies. Our findings also suggest that gain-of-toxicity mechanisms may be more
441 widespread in autosomal recessive diseases involving genes with paralogs.

442

443 ## Acknowledgments

444 We thank members of the Wu lab and the Cardiometabolic Genomics Program for discussion and
445 comments on the manuscript. This work is supported by NIH/NHLBI grant 1R01HL171664-01 and
446 Pershing Square Foundation MIND Prize (X.W.) and a postdoctoral fellowship from American Heart
447 Association (M.R.M). This research was funded in part through the NIH/NCI Cancer Center Support
448 Grant P30CA013696 and used the Genomics and High Throughput Screening Shared Resource and

449 CCTI Flow Cytometry Core. The CCTI Flow Cytometry Core is supported in part by the Office of the
450 Director, National Institutes of Health under awards S10OD030282 and S10OD020056.

451 Author contributions

452 X.W. and M.R.M. conceived the functional study and wrote the manuscript with input from all
453 authors. M.R.M. performed the majority of experiments. M.G. coordinated case reports and
454 sample collection. T.M.L. and J.M.F. identified and characterized the D308N/T340Nfs*26 case.
455 M.V.P., A.B., and P.J. identified and characterized the D308N/R58Q case. R.K.S. generated the
456 proteomics data. Y.Y. assisted in imaging. W.K.C. contributed the D308N/T189M tissue sample.
457 W.K.C., M.P.R., and F.Y. edited the manuscript and provided critical feedback.

458 Declaration of interests

459 X.W. is a member of the Scientific Advisory Board for Epitor Therapeutics. W.K.C. serves on the
460 Board of Directors at Prime Medicine.

461

462 Materials and Methods

463 Cell Culture, Drugs and Transfection

464 AC16 cells were cultured at 37°C, 5% CO_2 in low-glucose DMEM (Fisher; 11-885-084)
465 supplemented with 10% FBS. HEK293T cells were cultured in DMEM with 10% FBS. For
466 immunofluorescence assays, 2 x 10^5 cells were plated in 6 well plates and incubated for 24 hours.
467 For stable cell generation, EZ-Tet-RPL3-shRNA was co-transfected with CMV-dR8.91 and MD2.G
468 plasmids for 72 hours in HEK293T cells to produce virus. The media was centrifuged for 5 minutes
469 at RT, filtered using 0.45µm Syringe Filter Unit (Fisher), and 200µl viral media was added to 2 x 10^5
470 AC16 cells for 48 hours prior to selection using 200µg/ml Hygromycin B until control cells (non-
471 transduced) were dead. For stable generation of pLenti-RPL3L, procedure was followed as above
472 except transduction was carried out on EZ-Tet-RPL3-shRNA/AC16 cells and selection was carried
473 out by sorting for BV421-positive cells. For mRNA stability assay, AC16 cells were treated with
474 50mg/ml a-amanitin for the indicated time points.
475

476 Plasmids

477 To generate plasmid expressing shRNA against RPL3, a reported high efficiency shRNA sequence
478 for RPL3 was identified (Sigma) and ~70nt single stranded oligos were ordered from IDT and
479 annealed by heating to 95°C and cooled at a rate of 5°C min^{-1}. Double-stranded oligos had two 5'
480 overhangs corresponding to NheI and EcoRI sites, respectively. dsDNA oligos were ligated to EZ-
481 Tet-pLKO-Hygro (Addgene; 85972) using Quick Ligation Kit (NEB), producing Tet-inducible RPL3
482 shRNA vector. The pLenti-RPL3L plasmid was derived from pLentiRNACRISPR_007 (Addgene;
483 138149). A gene fragment containing the wild-type human RPL3L sequence with a C-terminal HA
484 tag was delivered on pUC57 (Genewiz). PCR products for wild-type RPL3L-HA derived from pUC57,
485 the pLentiRNACRISPR_007 backbone, and EBFP (unpublished in-house plasmid) with overlapping
486 ends were assembled via Gibson cloning using NEBuilder HiFi DNA Assembly Master Mix (NEB),

487 producing Dox-inducible RPL3L and constitutive EBFP expression. To obtain RPL3L mutation
488 plasmids, primers (Supplementary Table) were designed against pUC57-RPL3L-HA with single
489 nucleotide substitutions in the 5' region of the forward primer sequence. Mutagenesis was
490 performed using Site Directed Mutagenesis Kit (NEB) as per the manufacturer's instructions.
491 pLenti-RPL3L mutations were derived similarly to the wild-type as above.
492
493 Immunofluorescence and FISH
494 15,000 cells were seeded on Lab-Tek II (Thermo) chamber slides and grown overnight. Cells were
495 washed once with PBS and fixed in 300µl PFA at room temperature for 15 minutes. Fixed wells
496 were washed 3x with PBS for 3 minutes, permeabilized in 0.5% Triton X-100 in PBS for 15 minutes,
497 washed 3x, and incubated in 3% BSA in PBS for 1 hour to block. Cells were then incubated in 3%
498 BSA containing primary antibody overnight at 4°C, washed 3x in PBS, then incubated for 1 hour at
499 room temperature in secondary antibody protected from light. After washing 3x, cells were
500 incubated in 1:1000 DAPI solution for 5 minutes, washed 3x, then imaged using a Nikon Eclipse Ti
501 Series confocal microscope equipped with 60x lens performed at Columbia University's Confocal
502 and Specialized Microscopy Core. RPL3L was detected using anti-HA (Thermo; 2-2.2.14).
503 Secondary staining was accomplished using goat anti-rabbit IgG (H+L) Alexa Fluor 488 (Invitrogen)
504 and goat anti-mouse IgG (H+L) Alexa Fluor 594 (Invitrogen). For rRNA FISH, cells were fixed as
505 above but permeabilized with 70% ethanol for at least 1 hr. Custom designed 28S rRNA FISH
506 probes (Supplementary Table) were designed conjugated to CAL Fluor® Red 590 dye (Stellaris) and
507 incubated with fixed samples for 16 hours in the dark. After washing using wash buffers A + B
508 (Stellaris), samples were incubated with primary anti-HA antibody as above.
509
510 Polysome fractionation
511 Sucrose gradient density ultracentrifugation was used to separate the monosomal and polysomal
512 ribosomal fractions. For human cell experiments, AC16 cells were grown in 15cm dish were lysed
513 by adding 800µl of ice-cold lysis buffer (20mM HEPES, 150mM KCl, 10mM $MgCl_2$), plus 0.5% NP-
514 40, 1x EDTA-free Protease Inhibitor Cocktail (PIC; Roche)), 2.5mM DTT, 25 U ml^{-1} Turbo DNase I
515 (Invitrogen)), 10U SuperaseIN (Thermo), 2mM Vanadyl Ribonucleoside Complex (NEB) and
516 100ug/ml CHX (Sigma) directly to the plate and scraping. Lysed material was transferred to 1.5ml
517 centrifuge tube then triturated 10x with 23-gauge syringe. Samples were incubated in 4ºC for 30
518 minutes with rotation to complete lysis, then centrifuged at 14,000g for 7 minutes. Supernatant
519 was transferred to new tube and 700ul of lysate was loaded onto a 10-50% sucrose gradient,
520 before ultracentrifugation at 38,000rpm for 2 hours. The sucrose gradient was made by combining
521 10% and 50% sucrose solutions in lysis buffer, plus 2.5mM DTT, 160U SuperaseIN, and 100µg/ml
522 CHX. Both gradient formation and fractionation was performed on a Biocomp Gradient Profiler
523 (Biocomp). For protein extraction post-fractionation, 1 volume of TCA to 4 volumes of protein
524 sample was added, incubated for 10 minutes on ice, then span at 14,000rpm for 5 minutes at 4°C.
525 Pellet was washed twice with ice-cold acetone and dried at 95°C for 5 minutes. For SDS-PAGE, 4x
526 Sample reducing agent (GenScript) diluted 1:1 in RIPA was added to dry pellet and heated for an
527 additional 5 minutes at 95°C.
528
529 Western blotting

530 Western blot analysis was performed after SDS-PAGE using standard protocols. The antibodies
531 used were anti-HA (Thermo; 2-2.2.14), anti-RPL3 (Sigma; 3365), anti-RPL28 (Invitrogen; 62192),
532 anti-RPS3 (Thermo; 2G7H4), anti-GAPDH (Invitrogen; PA1988), and anti-Vinculin (CST; E1E9V).
533

534 RNA extraction/analysis and qPCR

535 Total RNA was isolated using NucleoSpin RNA Plus kit (Macharey-Nagel) including use of gDNA
536 removal column. For rRNA analysis, 500ng RNA was ran on 2100 Bioanalyzer (Agilent) at the
537 Columbia University's Molecular Pathology Core. For qPCR, cDNA synthesis was performed using
538 500ng RNA with the SuperScript IV Reverse Transcriptase (Invitrogen) as per the manufacturers
539 protocol with oligo(dT) primers. Real-time PCR was carried out using PowerUp SYBR Green Master
540 Mix using 1:3 diluted cDNA. For qRT-PCR, triplicates were performed with 0.5µM primer and 1µl
541 cDNA per reaction in the QuantStudio 7 Flex Real-Time PCR System. Ct values obtained were
542 plotted using GAPDH mRNA as loading control. Quantifications were performed as per the MIQE
543 guidelines. Statistical tests were performed with Prism 9 and two-sided Student's t-test were used
544 to calculate the *P* values. Data are expressed as mean ± s.d. for the number of replicates indicated,
545 with $P < 0.01$ considered significant. All primer sequences are displayed in Supplementary Table.

546 Nuclear/Cytoplasmic RNA Extraction Protocol

547 Cells were washed with ice-cold PBS, scraped into 1.7ml tubes, and pelleted at 500 g for 5 minutes
548 at 4°C. Cytoplasmic RNA was extracted by lysing cells in Cytoplasmic Lysis Buffer (40 mM HEPES-
549 NaOH pH 7.5, 160 mM KCl, 10 mM $MgCl_2$, 0.5% NP-40, 0.5% glycerol, and SuperaseIn) for 30
550 minutes at 4°C with rotation, followed by centrifugation at 2000 g for 2 minutes to separate the
551 cytoplasmic supernatant. Nuclear pellets were washed in Cytoplasmic Lysis Buffer (without
552 detergent), centrifuged at 500 g for 5 minutes, and subjected to a wash with Nuclear Lysis Buffer
553 (10 mM Tris-HCl pH 8.0, 1.5 mM KCl, 2.5 mM $MgCl_2$, 5% glycerol, 0.5% Triton X-100, 0.5%
554 deoxycholate, and 20U SuperaseIN) for 15 minutes at 4°C. Final washes were performed with
555 Cytoplasmic Lysis Buffer (without detergent), and nuclei were pelleted at 2000 g for 2 minutes.
556 Both cytoplasmic and nuclear RNA were extracted as above.

557 Co-immunoprecipitation

558 To prepare magnetic bead-antibody complex, 50µl of Dynabeads Protein G (Invitrogen) was
559 washed 3x with lysis buffer then incubated with 5µl anti-HA (Thermo; 2-2.2.14) in 400µl lysis buffer
560 for 1 hour at RT with constant rotation. Magnetic bead-antibody complex was captured using
561 Magnetic Separation Rack (NEB), washed 2x with cytoplasmic lysis buffer (20mM Tris-HCl, pH 7.5,
562 150mM KCl, 10% glycerol and 0.1% NP-40) then 3x with lysis buffer. 2x 15cm plates at 80%
563 confluency were grown, cells were washed twice in ice-cold PBS and 400µl of ice-cold lysis buffer
564 was dripped onto the plate and scraped, incubated in microcentrifuged tubes after triturating 10x
565 with 23-gauge syringe, and centrifuged at 14,000g for 7 minutes. The supernatant was added to
566 bead-antibody complex and incubated with rotation at 4°C overnight. Next day, bead-antibody-
567 antigen complex was washed 3x for 10 minutes at 4°C with ice-cold lysis buffer. Protein was eluted
568 by incubation with 40µl pH 3 glycine and heating at 70°C with shaking for 10 minutes, then
569 neutralized with 1/10 volume pH 8.0 Tris.
570

571 Proteomics
572 Explanted frozen patient tissue was homogenized with pestle and mortar under liquid nitrogen
573 and lysed in RIPA for mass spectrometric analysis by the Proteomics core facility at Columbia.
574 PASEF[64] based proteomics was employed. Briefly, proteins were denatured in 0.5% sodium
575 deoxycholate (SDC) buffer containing 100 mM Tris-HCl (pH 8.5). Samples were boiled for 20
576 minutes at 60°C with agitation (1000 rpm). Protein reduction and alkylation of cysteine residues
577 were performed using 10 mM tris(2-carboxyethyl)phosphine (TCEP) and 40 mM chloroacetamide
578 (CAA) at 45°C for 15 minutes. Following sonication in a water bath and cooling to room
579 temperature, and cleanup with the SP3 method[65]. Proteins were digested overnight with a
580 LysC/trypsin mix at a 1:50 enzyme-to-protein ratio at 37°C and 1400 rpm. After digestion, peptides
581 were acidified with 1% trifluoroacetic acid (TFA), vortexed, and desalted using StageTip technology
582 with SDB-RPS (styrene-divinylbenzene reversed-phase sulfonate) resin. The cleaned peptides were
583 dried using a vacuum concentrator and resuspended in 10 µl of LC buffer (3% acetonitrile, 0.1%
584 formic acid). Peptide concentrations were measured using a NanoDrop spectrophotometer, and
585 150 ng of each sample was subjected to PASEF analysis on a timsTOF Pro2 mass spectrometer. For
586 liquid chromatography with tandem mass spectrometry (LC-MS/MS), peptides were separated
587 within 87 min at a flow rate of 300 nl/min on a reversed-phase C18 column with an integrated
588 CaptiveSpray Emitter (25 cm x 75µm, 1.6 µm, IonOpticks). Mobile phases A and B were with 0.1%
589 formic acid in water and 0.1% formic acid in ACN. The fraction of B was linearly increased from 2
590 to 23% within 60 min, followed by an increase to 35% within 7 min and a further increase to 90%
591 before re-equilibration. The timsTOFPro2 mass spectrometer was operated in Parallel
592 Accumulation Serial Fragmentation (PASEF) mode with the following parameters: a mass range of
593 100 to 1700 m/z, an ion mobility range of 1/K0 0.7 to 1.3 V·s/cm², a ramp time of 200 ms, and a
594 duty cycle locked to 100%. Additional settings included a capillary voltage of 1600 V, dry gas flow
595 rate of 3 L/min, and a dry temperature of 180°C. PASEF data acquisition was configured for 10
596 MS/MS frames with a total duty cycle of 2.27 seconds, targeting a charge range of 0–5, an active
597 exclusion duration of 0.4 minutes, a target intensity of 20,000, and an intensity threshold of 2500.
598 Collision-induced dissociation (CID) was performed with a collision energy of 59 eV. A polygon filter
599 was applied in the m/z and ion mobility dimensions to prioritize features likely representing
600 peptide precursors and exclude singly charged background ions. For LC-MS/MS data analysis,
601 acquired PASEF raw files were analyzed using the MaxQuant environment V.2.2.0.0 and
602 Andromeda for database searches at default settings with a few modifications[66]. The default is
603 used for the first search tolerance and main search tolerance (20 ppm and 4.5 ppm, respectively).
604 MaxQuant was set up to search with the reference human proteome database downloaded from
605 UniProt. MaxQuant performed the search trypsin digestion with up to 2 missed cleavages. Peptide,
606 site, and protein false discovery rates (FDR) were all set to 1% with a minimum of 1 peptide needed
607 for identification; label-free quantitation (LFQ) was performed with a minimum ratio count of 1.
608 The following modifications were used for protein identification and quantification:
609 Carbamidomethylation of cysteine residues (+57.021 Da) was set as static modifications, while the
610 oxidation of methionine residues (+15.995 Da), and deamidation (+0.984) on asparagine were set
611 as a variable modification. Results obtained from MaxQuant, protein groups table was further
612 used for data analysis. Custom fasta files containing mutant D308N peptides were analyzed on
613 MaxQuant for peptide abundance relative to wildtype peptide abundance. For nuclear IP of cell

614 lines, MaxQuant outputs were analyzed using Differential Expression of Proteins (DEP) package in
615 R.
616
617 Chromatin Immunoprecipitation (ChIP)
618 Cells were crosslinked with 1% formaldehyde in the culture medium for 15 minutes at room
619 temperature, followed by quenching with 125 mM glycine for 5 minutes. Cells were pelleted and
620 washed. The pellet was resuspended in RIPA buffer with protease inhibitor cocktail (Roche),
621 incubated on ice, and sonicated to shear chromatin (~1 kb fragments). The lysate was centrifuged
622 at 12,000 x g for 10 minutes at 4 °C, and the volume was increased with dilution buffer (165 mM
623 NaCl, 0.01% SDS, 1.1% Triton X-100, 1.2 mM EDTA, 16.7 mM Tris–HCl, pH 8.0). Chromatin was
624 incubated with 5 µg of anti-RNAPII (Santa Cruz; F-12) for overnight at 4 °C. Chromatin-Antibody
625 mix was incubated with pre-washed Dynabeads and incubated at RT for 45 minutes. Beads were
626 washed 5x in dilution buffer and eluted in genomic DNA extraction kit (Macharey-Nagel) lysis
627 buffer, resuspended in 50 µL of water. PCR was performed using purified DNA and compared to
628 input samples. Two-sided Student's t-tests were carried out to calculate *P* value.

629 Nuclear localization calculation
630 Nuclear localization was calculated as a ratio of the immunofluorescent co-localization signal of
631 anti-HA with nuclear regions compared to anti-HA signal with cytoplasmic regions, determined as
632 cellular regions lacking in DAPI signal. The same calculation was performed for 28S rRNA. All
633 calculations were carried out with ImageJ. Cytoplasmic/Nuclear signal ratios for each cell were
634 compiled and underwent one-way ANOVA with Dunnett correction for multiple comparisons
635 across conditions.
636
637 Tissue RNA-seq
638 Explanted frozen patient heart tissue was homogenized using pestle and mortar under liquid
639 nitrogen. Homogenized tissue was submerged in TRIzol and extracted using Direct-zol kit (Zymo
640 Research). RNA integrity was analyzed with Bioanalyzer electrophoresis. Samples underwent
641 poly(A) RNA pulldown and libraries were constructed using Illumina TruSeq chemistry. Libraries
642 were sequenced at Columbia Sulzberger Genome Center with NovaSeq 6000 (Illumina). RTA
643 (Illumina) was used for base calling and bcl2fastq2 (version 2.19) for converting BCL to fastq format.
644 Gene expression was quantified using kallisto with a customized transcriptome index (human
645 MANE select). RNA-seq data for three age-matched control samples were downloaded from
646 European Nucleotide Archive (ENA project PRJEB26969, sample ID: 5818sTS, 5828sTS, and
647 5836sTS) and analyzed similarly. DESeq2 was used for differential gene expression analysis.
648
649
650 References

651 1. Bergmann, O. et al. Dynamics of Cell Generation and Turnover in the Human Heart. Cell
652 161, 1566-1575 (2015).
653 2. Van Raay, T.J., Connors, T.D., Klinger, K.W., Landes, G.M. & Burn, T.C. A novel ribosomal
654 protein L3-like gene (RPL3L) maps to the autosomal dominant polycystic kidney disease
655 gene region. Genomics 37, 172-176 (1996).

656 3. Chaillou, T., Zhang, X. & McCarthy, J.J. Expression of Muscle-Specific Ribosomal Protein L3-
657 Like Impairs Myotube Growth. J Cell Physiol 231, 1894-1902 (2016).
658 4. Shiraishi, C. et al. RPL3L-containing ribosomes determine translation elongation dynamics
659 required for cardiac function. Nat Commun 14, 2131 (2023).
660 5. Gay, D.M., Lund, A.H. & Jansson, M.D. Translational control through ribosome
661 heterogeneity and functional specialization. Trends Biochem Sci 47, 66-81 (2022).
662 6. Genuth, N.R. et al. A stem cell roadmap of ribosome heterogeneity reveals a function for
663 RPL10A in mesoderm production. Nat Commun 13, 5491 (2022).
664 7. Genuth, N.R. & Barna, M. The Discovery of Ribosome Heterogeneity and Its Implications
665 for Gene Regulation and Organismal Life. Mol Cell 71, 364-374 (2018).
666 8. Simsek, D. et al. The Mammalian Ribo-interactome Reveals Ribosome Functional Diversity
667 and Heterogeneity. Cell 169, 1051-1065 e1018 (2017).
668 9. Shi, Z. et al. Heterogeneous Ribosomes Preferentially Translate Distinct Subpools of mRNAs
669 Genome-wide. Mol Cell 67, 71-83 e77 (2017).
670 10. Li, H. et al. A male germ-cell-specific ribosome controls male fertility. Nature 612, 725-731
671 (2022).
672 11. Zou, Q. et al. Proteostasis regulated by testis-specific ribosomal protein RPL39L maintains
673 mouse spermatogenesis. iScience 24, 103396 (2021).
674 12. Meskauskas, A., Harger, J.W., Jacobs, K.L. & Dinman, J.D. Decreased peptidyltransferase
675 activity correlates with increased programmed -1 ribosomal frameshifting and viral
676 maintenance defects in the yeast Saccharomyces cerevisiae. RNA 9, 982-992 (2003).
677 13. Burn, T.C. et al. Generation of a transcriptional map for a 700-kb region surrounding the
678 polycystic kidney disease type 1 (PKD1) and tuberous sclerosis type 2 (TSC2) disease genes
679 on human chromosome 16p3.3. Genome Res 6, 525-537 (1996).
680 14. Litvinukova, M. et al. Cells of the adult human heart. Nature 588, 466-472 (2020).
681 15. Consortium, G.T. The GTEx Consortium atlas of genetic regulatory effects across human
682 tissues. Science 369, 1318-1330 (2020).
683 16. Grimes, K.M. et al. Rpl3l gene deletion in mice reduces heart weight over time. Frontiers
684 in Physiology 14 (2023).
685 17. Milenkovic, I. et al. RPL3L-containing ribosomes modulate mitochondrial activity in the
686 mammalian heart. bioRxiv, 2021.2012.2004.471171 (2021).
687 18. Ganapathi, M. et al. Bi-allelic missense disease-causing variants in RPL3L associate neonatal
688 dilated cardiomyopathy with muscle-specific ribosome biogenesis. Hum Genet 139, 1443-
689 1454 (2020).
690 19. Das, B.B., Gajula, V., Arya, S. & Taylor, M.B. Compound Heterozygous Missense Variants in
691 RPL3L Genes Associated with Severe Forms of Dilated Cardiomyopathy: A Case Report and
692 Literature Review. Children (Basel) 9 (2022).
693 20. Nannapaneni, H. et al. Further Evidence of Autosomal Recessive Inheritance of RPL3L
694 Pathogenic Variants with Rapidly Progressive Neonatal Dilated Cardiomyopathy. J
695 Cardiovasc Dev Dis 9 (2022).
696 21. Al-Hassnan, Z.N. et al. Categorized Genetic Analysis in Childhood-Onset Cardiomyopathy.
697 Circ Genom Precis Med 13, 504-514 (2020).

698 22. Bajpai, A.K. et al. Exploring the Regulation and Function of Rpl3l in the Development of
699 Early-Onset Dilated Cardiomyopathy and Congestive Heart Failure Using Systems Genetics
700 Approach. Genes (Basel) 15 (2023).
701 23. Yang, Q. et al. Novel compound heterozygous variants in the RPL3L gene causing dilated
702 cardiomyopathy type-2D: a case report and literature review. BMC Med Genomics 16, 127
703 (2023).
704 24. McNally, E.M. & Mestroni, L. Dilated Cardiomyopathy: Genetic Determinants and
705 Mechanisms. Circ Res 121, 731-748 (2017).
706 25. Rosenbaum, A.N., Agre, K.E. & Pereira, N.L. Genetics of dilated cardiomyopathy: practical
707 implications for heart failure management. Nat Rev Cardiol 17, 286-297 (2020).
708 26. Kamisago, M. et al. Mutations in sarcomere protein genes as a cause of dilated
709 cardiomyopathy. N Engl J Med 343, 1688-1696 (2000).
710 27. Milenkovic, I. et al. Dynamic interplay between RPL3- and RPL3L-containing ribosomes
711 modulates mitochondrial activity in the mammalian heart. Nucleic Acids Res 51, 5301-5324
712 (2023).
713 28. Brown, L.P. & McCarthy, J.J., Vol. PhD (University of Kentucky, 2021).
714 29. Di Fede, G. et al. A recessive mutation in the APP gene with dominant-negative effect on
715 amyloidogenesis. Science 323, 1473-1477 (2009).
716 30. Chen, S. et al. A genomic mutational constraint map using variation in 76,156 human
717 genomes. Nature 625, 92-100 (2024).
718 31. Cheng, J. et al. Accurate proteome-wide missense variant effect prediction with
719 AlphaMissense. Science 381, eadg7492 (2023).
720 32. Jumper, J. et al. Highly accurate protein structure prediction with AlphaFold. Nature 596,
721 583-589 (2021).
722 33. Bick, A.G. et al. Genomic data in the All of Us Research Program. Nature 627, 340-346
723 (2024).
724 34. Bycroft, C. et al. The UK Biobank resource with deep phenotyping and genomic data.
725 Nature 562, 203-209 (2018).
726 35. Thorolfsdottir, R.B. et al. Coding variants in RPL3L and MYZAP increase risk of atrial
727 fibrillation. Commun Biol 1, 68 (2018).
728 36. Sun, K.Y. et al. A deep catalogue of protein-coding variation in 983,578 individuals. Nature
729 631, 583-592 (2024).
730 37. Dorner, K., Ruggeri, C., Zemp, I. & Kutay, U. Ribosome biogenesis factors-from names to
731 functions. EMBO J 42, e112699 (2023).
732 38. Adamo, L., Rocha-Resende, C., Prabhu, S.D. & Mann, D.L. Reappraising the role of
733 inflammation in heart failure. Nat Rev Cardiol 17, 269-285 (2020).
734 39. Davidson, M.M. et al. Novel cell lines derived from adult human ventricular cardiomyocytes.
735 J Mol Cell Cardiol 39, 133-147 (2005).
736 40. Hedaya, O.M. et al. Secondary structures that regulate mRNA translation provide insights
737 for ASO-mediated modulation of cardiac hypertrophy. Nat Commun 14, 6166 (2023).
738 41. Guo, Y. & Pu, W.T. Cardiomyocyte Maturation: New Phase in Development. Circ Res 126,
739 1086-1106 (2020).

740 42. Thomas, D., Cunningham, N.J., Shenoy, S. & Wu, J.C. Human-induced pluripotent stem cells
741 in cardiovascular research: current approaches in cardiac differentiation, maturation
742 strategies, and scalable production. Cardiovasc Res 118, 20-36 (2022).
743 43. Pillet, B. et al. Dedicated chaperones coordinate co-translational regulation of ribosomal
744 protein production with ribosome assembly to preserve proteostasis. Elife 11 (2022).
745 44. Iouk, T.L., Aitchison, J.D., Maguire, S. & Wozniak, R.W. Rrb1p, a yeast nuclear WD-repeat
746 protein involved in the regulation of ribosome biosynthesis. Mol Cell Biol 21, 1260-1271
747 (2001).
748 45. Schaper, S. et al. A yeast homolog of chromatin assembly factor 1 is involved in early
749 ribosome assembly. Curr Biol 11, 1885-1890 (2001).
750 46. Bhutada, P. et al. Rbp95 binds to 25S rRNA helix H95 and cooperates with the Npa1
751 complex during early pre-60S particle maturation. Nucleic Acids Res 50, 10053-10077
752 (2022).
753 47. Sailer, C. et al. A comprehensive landscape of 60S ribosome biogenesis factors. Cell Rep 38,
754 110353 (2022).
755 48. Ismail, S. et al. Emergence of the primordial pre-60S from the 90S pre-ribosome. Cell Rep
756 39, 110640 (2022).
757 49. De Marchis, M.L., Giorgi, A., Schinina, M.E., Bozzoni, I. & Fatica, A. Rrp15p, a novel
758 component of pre-ribosomal particles required for 60S ribosome subunit maturation. RNA
759 11, 495-502 (2005).
760 50. Tafforeau, L. et al. The complexity of human ribosome biogenesis revealed by systematic
761 nucleolar screening of Pre-rRNA processing factors. Mol Cell 51, 539-551 (2013).
762 51. Bruning, L. et al. RNA helicases mediate structural transitions and compositional changes
763 in pre-ribosomal complexes. Nat Commun 9, 5383 (2018).
764 52. Rodriguez-Mateos, M. et al. Role and dynamics of the ribosomal protein P0 and its related
765 trans-acting factor Mrt4 during ribosome assembly in Saccharomyces cerevisiae. Nucleic
766 Acids Res 37, 7519-7532 (2009).
767 53. Lee, T.M. et al. Pediatric Cardiomyopathies. Circ Res 121, 855-873 (2017).
768 54. Towbin, J.A. et al. Incidence, causes, and outcomes of dilated cardiomyopathy in children.
769 JAMA 296, 1867-1876 (2006).
770 55. Lipov, A. et al. Exploring the complex spectrum of dominance and recessiveness in genetic
771 cardiomyopathies. Nat Cardiovasc Res 2, 1078-1094 (2023).
772 56. Bamshad, M.J., Nickerson, D.A. & Chong, J.X. Mendelian Gene Discovery: Fast and Furious
773 with No End in Sight. Am J Hum Genet 105, 448-455 (2019).
774 57. Young, L.C. et al. Destabilizing NF1 variants act in a dominant negative manner through
775 neurofibromin dimerization. Proc Natl Acad Sci U S A 120, e2208960120 (2023).
776 58. Utsumi, T. et al. Exclusive Characteristics of the p.E555K Dominant-Negative Variant in
777 Autosomal Dominant E47 Deficiency. J Clin Immunol 44, 167 (2024).
778 59. Boettcher, S. et al. A dominant-negative effect drives selection of TP53 missense mutations
779 in myeloid malignancies. Science 365, 599-604 (2019).
780 60. Gerasimavicius, L., Livesey, B.J. & Marsh, J.A. Loss-of-function, gain-of-function and
781 dominant-negative mutations have profoundly different effects on protein structure. Nat
782 Commun 13, 3895 (2022).

783 61. El-Brolosy, M.A. et al. Genetic compensation triggered by mutant mRNA degradation.
784 Nature 568, 193-197 (2019).
785 62. Rossi, A. et al. Genetic compensation induced by deleterious mutations but not gene
786 knockdowns. Nature 524, 230-233 (2015).
787 63. El-Brolosy, M.A. & Stainier, D.Y.R. Genetic compensation: A phenomenon in search of
788 mechanisms. PLoS Genet 13, e1006780 (2017).
789 64. Meier, F. et al. Online Parallel Accumulation-Serial Fragmentation (PASEF) with a Novel
790 Trapped Ion Mobility Mass Spectrometer. Mol Cell Proteomics 17, 2534-2545 (2018).
791 65. Soni, R.K. Protocol for deep proteomic profiling of formalin-fixed paraffin-embedded
792 specimens using a spectral library-free approach. STAR Protoc 4, 102381 (2023).
793 66. Cox, J. et al. Andromeda: A Peptide Search Engine Integrated into the MaxQuant
794 Environment. Journal of Proteome Research 10, 1794-1805 (2011).
795

796 ## Figure legends

797 **Figure 1. Hotspot G27D and D308N/V are potential driver mutations in *RPL3L*-linked DCM. a**,
798 Schematic of neonatal DCM-causing mutations across RPL3L protein. Each circle (missense) or
799 rectangle (frameshift) represents a mutation. Mutations are colored by family and compound
800 heterozygous mutations found in the same family are linked by dashed lines. Mutations found in
801 the two new cases reported here are highlighted with a star. Protein domains in RPL3L are also
802 labeled. The two hotspot mutations, G27D and D308N/V, are emphasized in bold. **b**, Positions of
803 the variants (highlighted in red) mapped onto the AlphaFold-predicted 3D structure of RPL3L. **c**,
804 RPL3L missense variants clustered into two groups by their allele frequency (gnomAD) and
805 predicted pathogenicity (AlphaMissense). Variants are colored and linked as in **a**. **d**, Putative
806 human *RPL3L* KO in the general population (gnomAD). LOF: loss-of-function.
807

808 **Figure 2. Ribosome defects in explanted patient hearts**. **a**, Bioanalyzer electrophoresis of total
809 RNA isolated from explanted patient heart ventricular tissue and a control sample (human AC16
810 cells). **b**, Differential gene expression analysis comparing explanted heart tissue (N=2)and age-
811 matched healthy control heart ventricular tissue (N=3). Genes encoding 60S or 40S ribosomal
812 proteins are colored red or blue, respectively. *RPL3* and *RPL3L* are highlighted by yellow circles. **c**,
813 Cumulative distribution function plots for three significant gene signatures. Red indicates genes of
814 interest and black indicates all other genes. The median log2 fold change (log2fc) and Kolmogorov–
815 Smirnov test P values are also shown. **d**, RNA-seq read coverage (BAM file visualized in IGV genome
816 browser) showing that both D308N and T189M alleles are equally expressed. **e**, Mass
817 spectrometry quantification of RPL3 (left), RPL3L (center), and total 60S proteins (right) relative
818 total 40S proteins in D308N/T189M patient ventricular tissue (N=2) and age-matched control
819 tissue (N=3). ** $P < 0.0001$. **f**, Intensity of the peptide containing the D308 residue in the T189M
820 variant and the peptide containing the N308 residue in the D308N variant normalized to the total
821 intensity in RPL3L. ns: not significant.

822 **Figure 3. Hotspot variants disrupt ribosome biogenesis and impairs cell viability**. **a**, Isogenic
823 AC16 human cardiomyocyte-like cell lines were generated to simultaneously knockdown (KD) RPL3

824 and overexpress HA-tagged RPL3L (or its variants) via a dox-inducible promoter. **b**, RPL3
825 knockdown after dox treatment. Total RNA was isolated from indicated cell lines and analyzed for
826 RPL3 levels. shScramble: cells expressing only a control scrambled shRNA. shRPL3: cells expressing
827 only the RPL3 targeting shRNA without RPL3L or its variants. RPL3L-WT/SNP/T189M/D308N: cells
828 with RPL3 KD and expresses either wild type or the indicated variant of RPL3L. **c**, Efficient
829 expression of RPL3L variants in AC16 cells after 120 hours Dox treatment. Total RNA isolated from
830 indicated cells was analyzed for RPL3L levels (N = 3 independent experiments). **d**, Bioanalyzer
831 electrophoresis on total RNA from indicated cell lines was quantified by ImageJ. **e**, Loss of
832 translation capacity in shRPL3 and D308N cells, but not control or T189M cells. RPL3+ (shScramble)
833 and RPL3L-expressing cells were separated by ultracentrifugation and fractionated in the presence
834 of cycloheximide (N = 3). **f**, Cell growth defects in D308N and shRPL3 cells. AC16-derived cells were
835 seeded at equal density and counted every 2 days (N = 4). The y-axis is shown on a logarithmic
836 scale. The percentage values represent the cell density at day 10 relative to the RPL3L-WT cell line.
837 **b ,c, f ,** Data are mean ± s.d. *: P < 0.05.
838
839 **Figure 4. Hotspot variants mislocalize and alter interactions with ribosome biogenesis factors**.
840 **a**, Cells were stained for anti-HA antibody (RPL3L and variants) and 28S rRNA FISH probes and
841 analyzed by 60x confocal microscopy. Scale bar = 50μm. **b**, Violin plot quantification of cytoplasmic
842 and nuclear abundances of HA (RPL3L) signals for indicated cell lines, measured per cell (N = 26-
843 41 cells). **c**, same as b but for 28S rRNA. One-way ANOVA was used for statistical analysis. **d**, PCA
844 analysis of the proteins co-immunoprecipitated with RPL3L variants. N=3. **e**, Enrichment of
845 GRWD1 and C7ORF50 in proteins co-immunoprecipitated with the hotspot variants D308N and
846 G27D compared to other variants. Peptide intensities are normalized by the median of all samples
847 and then log2-transformed. Error bars represent standard deviation. ns, not significant; ** P <
848 0.001; *** P < 0.0001; **** P < 0.00001.
849
850 **Figure 5. Non-hotspot variants drive post-transcriptional *RPL3* compensatory up-regulation**. **a**,
851 Compensatory increase of *RPL3* mRNA in R161W cells. DCM-associated *RPL3L* variants were
852 expressed for 120 hours in doxycycline and total RNA was extracted and analyzed for *RPL3* mRNA
853 levels (N = 3 independent experiments). **b**, Western blotting shows compensatory increase of RPL3
854 protein levels in R161W cells. Cells were treated as in (a) and whole-cell lysates were
855 immunoblotted with indicated antibodies (N = 3 independent experiments). **c**, No difference in
856 transcription activity in *RPL3* promoter assayed by ChIP-qPCR. Multiple primer pairs were used for
857 each region. An intergenic region upstream of *RPL3L* was used as a negative control of non-
858 transcribed region (N = 3). **d**, *RPL3* mRNA half-life is enhanced in R161W cells. *RPL3L*-expressing
859 variants were incubated with 50μg/ml RNA Polymerase II inhibitor α-amanitin for indicated
860 timepoints prior to analysis for *RPL3* mRNA relative to GAPDH, normalized to 0 hour (N = 3). **e**,
861 Compensatory *RPL3* mRNA increase occurs entirely in the cytoplasm in R161W cells. RNA
862 underwent subcellular fractionation for amplification of *RPL3* levels relative to GAPDH (N = 4).
863 **a,c,d,e**, Data are mean ± s.d. ns, not significant; * P < 0.01; *** P < 0.0001; **** P < 0.00001.
864
865 **Figure 6. Impaired protein synthesis in engineered compound heterozygous cells**. **a**, Cells stably
866 integrated with G27D, R161W, or both G27D and R161W were induced with dox for 144hrs.
867 Puromycin was added to 1uM final concentration for 30 minutes before cells were harvested for

868 Western blotting (N = 4). **b**, Quantification of puromycin incorporation. **c**, Quantification of RPL3
869 protein abundance. Data are mean ± s.d. ns, not significant; * P < 0.01.
870
871 **Extended Data Figure 1. iPSC cardiomyocytes (iPSC-CMs) do not express *RPL3L*.** Data was
872 analyzed from RNA-seq performed by Pozo et al (2022) comparing iPSC-CMs to fetal and adult
873 human heart.
874
875 **Extended Data Figure 2. The hotspot G27D variant mirrors the effects of D308N. a**, Cell growth
876 defect for G27D and R161W, as in **Fig. 3f**. **b**, Polysome fraction for G27D and R161W, as in **Fig. 3e**.
877 Data are mean ± s.d.
878
879 **Extended Data Figure 3. Enrichment of 60S ribosome biogenesis factors in proteins co-**
880 **immunoprecipitated with nuclear RPL3L variants.** Peptide intensities are normalized by the
881 median of all samples and then log2-transformed. Error bars represent standard deviation.
882
883 **Extended Data Figure 4. R161W does not incorporate into polysomes.** Monosome and
884 polysomal fractions from **Fig. 5** were isolated by TCA precipitation and immunoblotted for HA-tag.
885 Input (pre-ultracentrifugation) samples were loaded as controls.
886
887 **Extended Data Figure 5. No change in the expression of the *RPL3*-targeting shRNA in *RPL3L*-**
888 **expressing cells**. A custom annotation was used to detect shRNA hairpin from RNA-seq data
889 obtained from *RPL3L* variant-expressing cell lines. RPM, Reads per million (N = 3 biological
890 replicates). Error bars represent standard deviation. ns, not significant.
891
892 **Extended Data Figure 6. R161W does not induce higher *RPL3* intronic RNA as a proxy of**
893 **transcription levels**. Total RNA was isolated and cDNA was synthesized using random primers.
894 Primers targeting intron 3 and intron 9 of *RPL3* were used for amplification (N = 3). Error bars
895 represent standard deviation. ns, not significant.
896

Figure 1

a

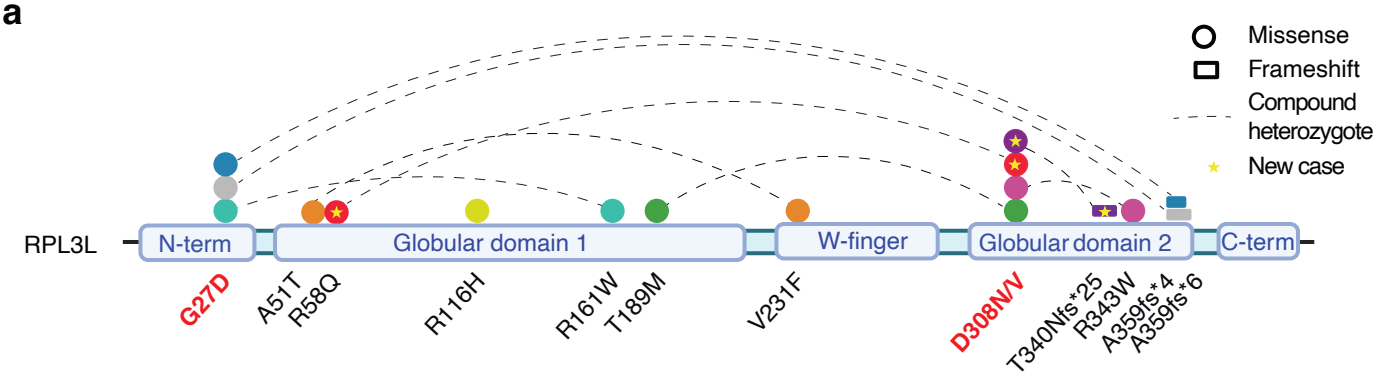

b

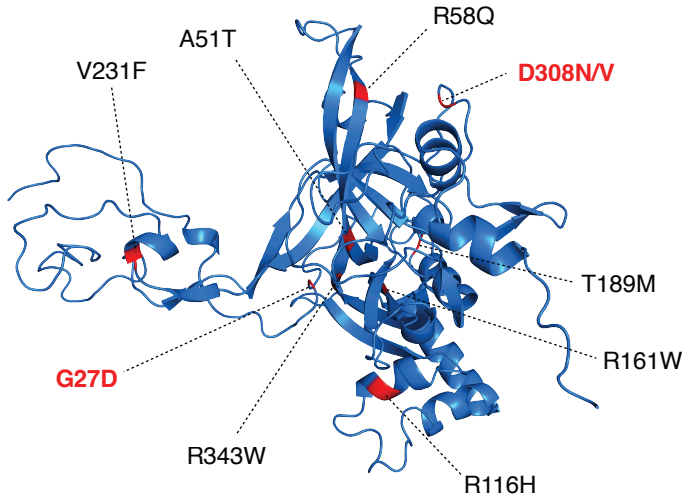

c

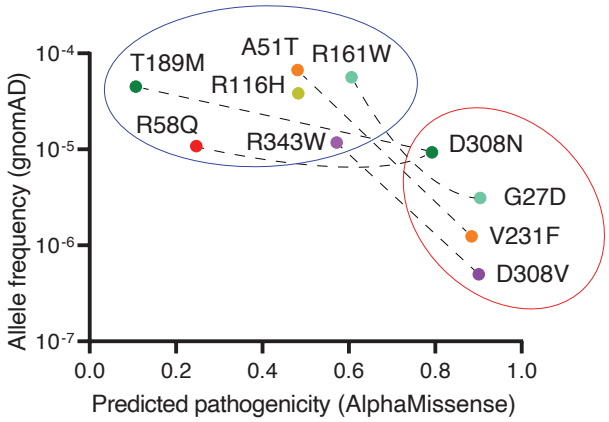

d

Putative LOF variant	Allele frequency	Homozygous humans
R226X (stop-gain)	1.67×10^{-5}	1 (gnomAD)
c.1167+1G>A (splice donor)	2.49×10^{-3}	9 (gnomAD)
	1.70×10^{-3}	2 (AllofUs)
	3.41×10^{-3}	6 (UK Biobank)

Figure 2

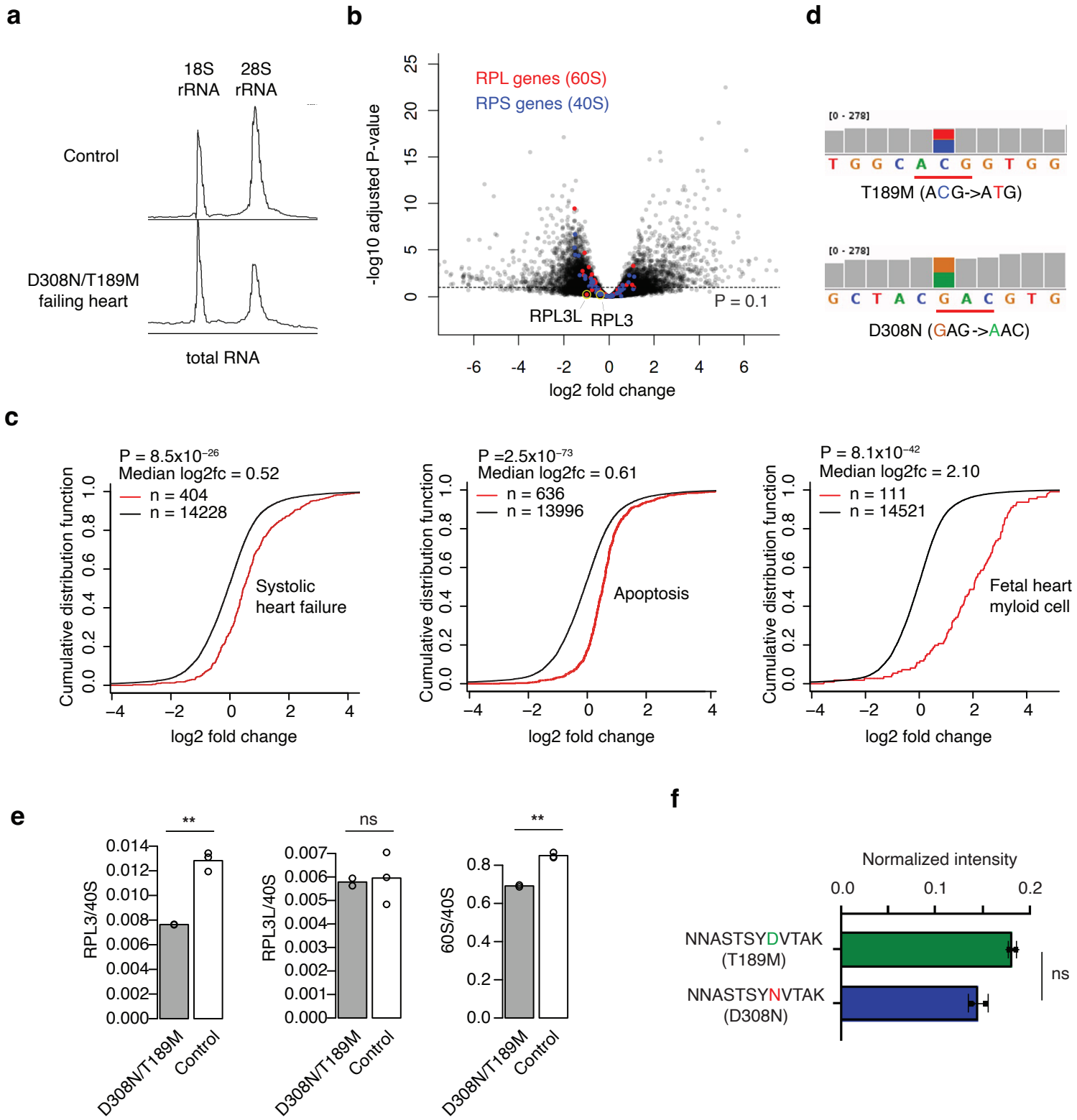
a
18S rRNA
28S rRNA
Control
D308N/T189M failing heart
total RNA
b
RPL genes (60S)
RPS genes (40S)
-log10 adjusted P-value
RPL3L
RPL3
P = 0.1
log2 fold change
d
[0 - 278]
T G G C A C G G T G G
T189M (ACG->ATG)
[0 - 278]
G C T A C G A C G T G
D308N (GAG->AAC)
c
P = 8.5x10^-26
Median log2fc = 0.52
n = 404
n = 14228
Systolic heart failure
Cumulative distribution function
log2 fold change
P =2.5x10^-73
Median log2fc = 0.61
n = 636
n = 13996
Apoptosis
P = 8.1x10^-42
Median log2fc = 2.10
n = 111
n = 14521
Fetal heart myloid cell
e
RPL3/40S
RPL3L/40S
60S/40S
**
ns
**
D308N/T189M
Control
f
Normalized intensity
NNASTSYDVTAK (T189M)
NNASTSYNVTAK (D308N)
ns

Figure 3

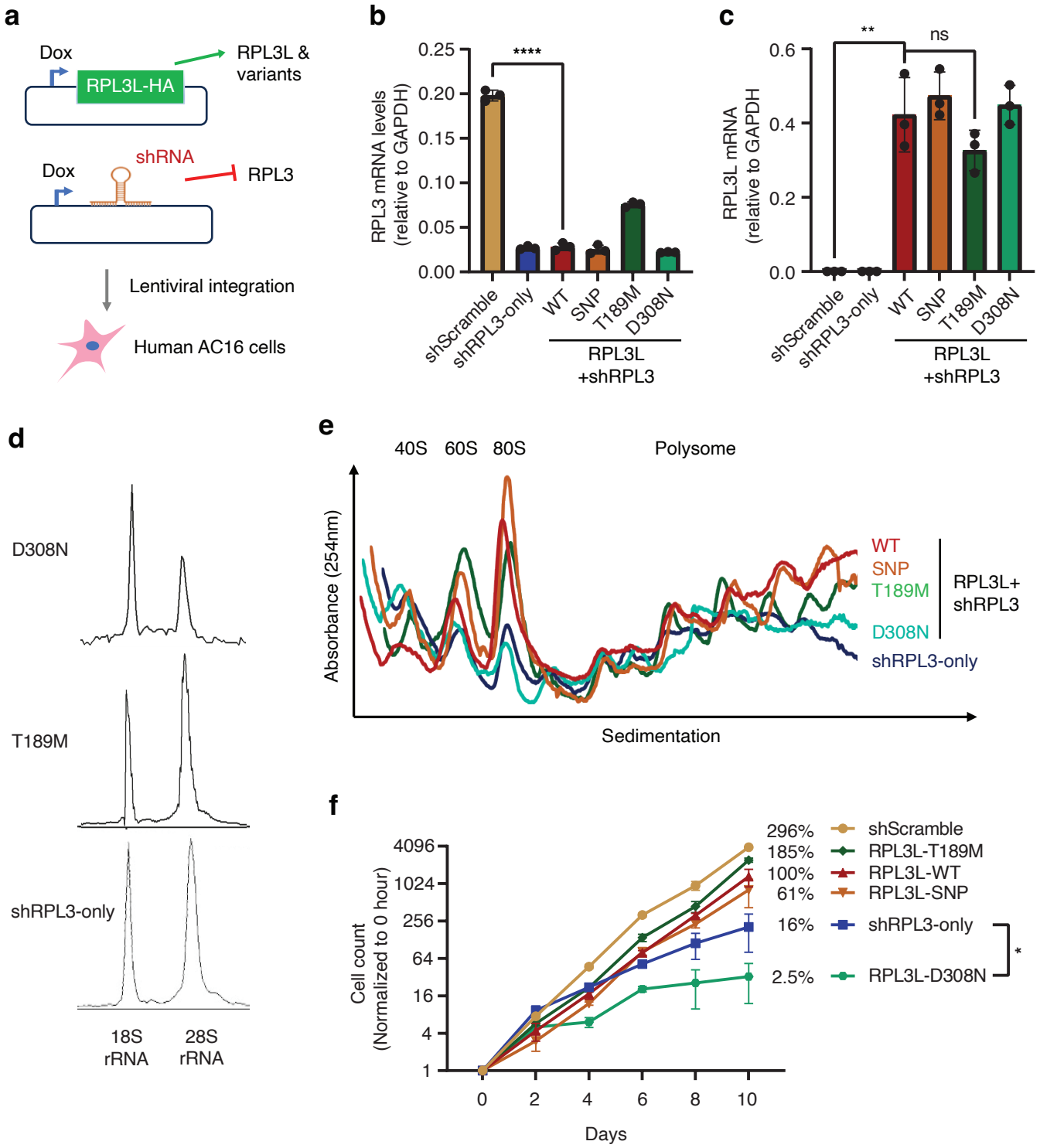
a
Dox
RPL3L-HA
RPL3L & variants
Dox
shRNA
RPL3
Lentiviral integration
Human AC16 cells
b
RPL3 mRNA levels (relative to GAPDH)
0.25
0.20
0.15
0.10
0.05
0.00
****
shScramble
shRPL3-only
WT
SNP
T189M
D308N
RPL3L +shRPL3
c
RPL3L mRNA (relative to GAPDH
0.6
0.4
0.2
0.0
**
ns
shScramble
shRPL3-only
WT
SNP
T189M
D308N
RPL3L +shRPL3
d
D308N
T189M
shRPL3-only
18S rRNA
28S rRNA
e
40S
60S
80S
Polysome
Absorbance (254nm)
Sedimentation
WT
SNP
T189M
D308N
RPL3L+ shRPL3
shRPL3-only
f
Cell count (Normalized to 0 hour)
4096
1024
256
64
16
4
1
0
2
4
6
8
10
Days
296% shScramble
185% RPL3L-T189M
100% RPL3L-WT
61% RPL3L-SNP
16% shRPL3-only
2.5% RPL3L-D308N
*

Figure 4

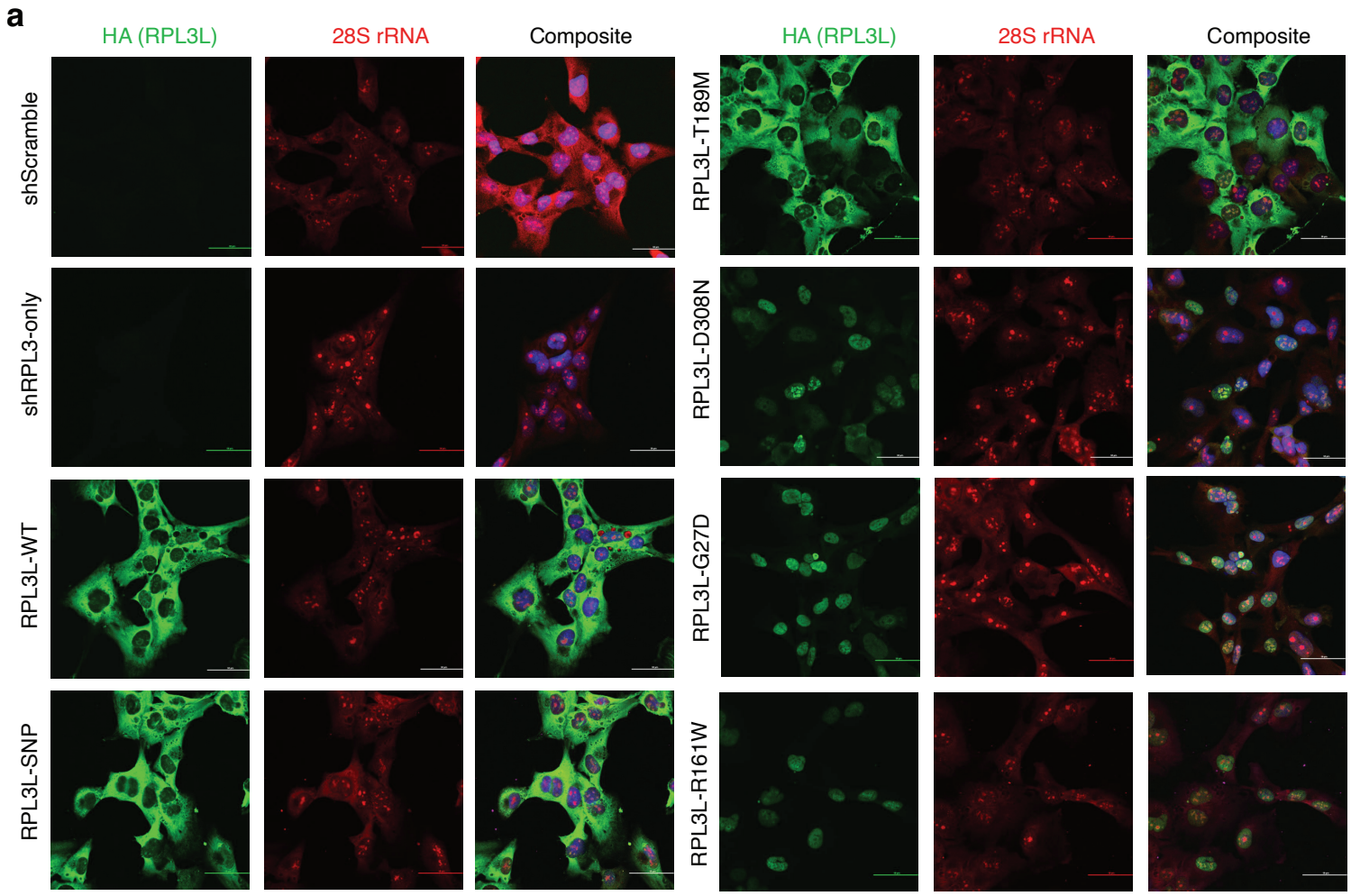
a
HA (RPL3L)
28S rRNA
Composite
shScramble
shRPL3-only
RPL3L-WT
RPL3L-SNP
RPL3L-T189M
RPL3L-D308N
RPL3L-G27D
RPL3L-R161W

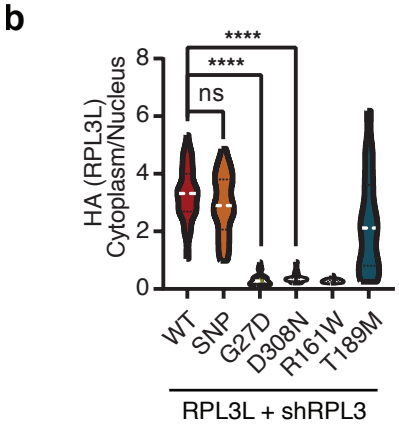
b
HA (RPL3L) Cytoplasm/Nucleus
****
****
ns
WT
SNP
G27D
D308N
R161W
T189M
RPL3L + shRPL3

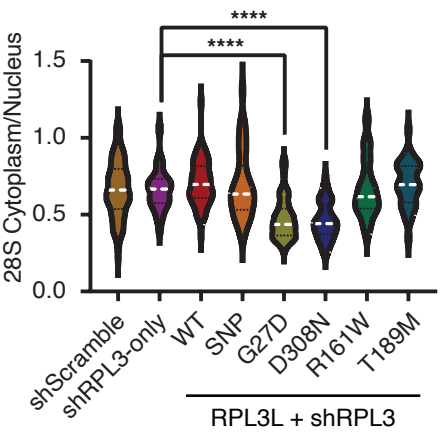
c
28S Cytoplasm/Nucleus
****
****
shScramble
shRPL3-only
WT
SNP
G27D
D308N
R161W
T189M
RPL3L + shRPL3

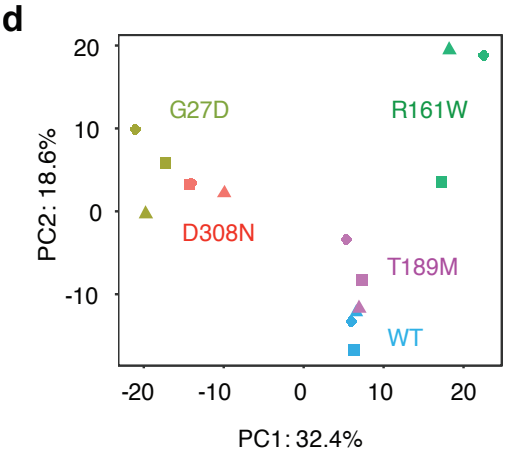
d
G27D
R161W
D308N
T189M
WT
PC2: 18.6%
PC1: 32.4%

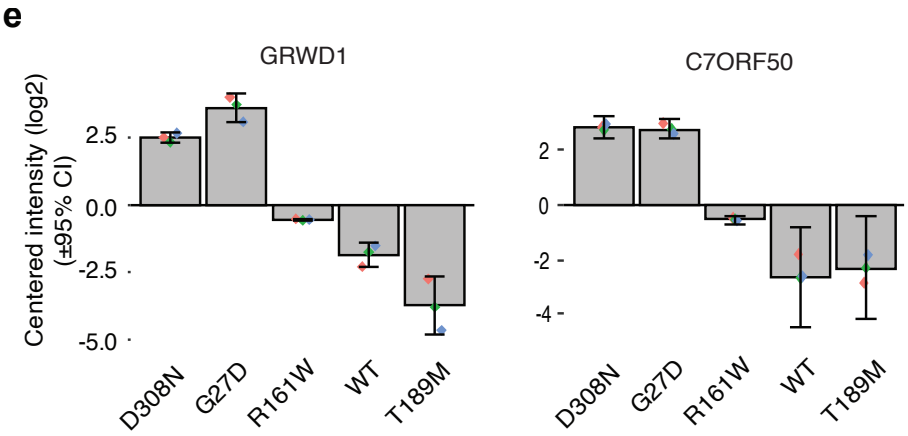
e
GRWD1
C7ORF50
Centered intensity (log2) (±95% CI)
D308N
G27D
R161W
WT
T189M

Figure 5

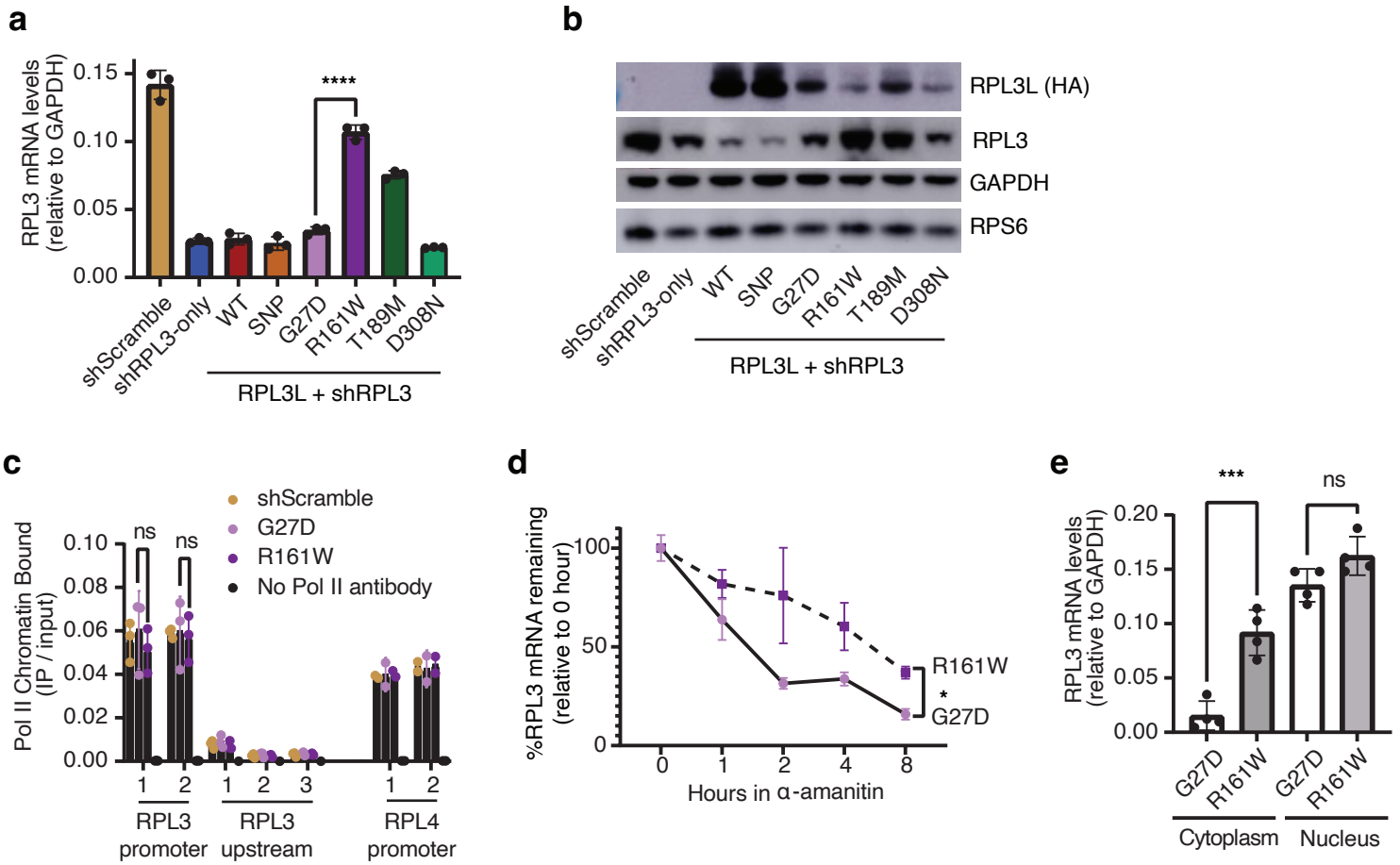
a
RPL3 mRNA levels (relative to GAPDH)
0.15
0.10
0.05
0.00
****
shScramble
shRPL3-only
WT
SNP
G27D
R161W
T189M
D308N
RPL3L + shRPL3
b
RPL3L (HA)
RPL3
GAPDH
RPS6
shScramble
shRPL3-only
WT
SNP
G27D
R161W
T189M
D308N
RPL3L + shRPL3
c
Pol II Chromatin Bound (IP / input)
0.10
0.08
0.06
0.04
0.02
0.00
ns
ns
shScramble
G27D
R161W
No Pol II antibody
1
2
1
2
3
1
2
RPL3 promoter
RPL3 upstream
RPL4 promoter
d
%RPL3 mRNA remaining (relative to 0 hour)
100
50
0
0
1
2
4
8
Hours in α-amanitin
R161W
*
G27D
e
RPL3 mRNA levels (relative to GAPDH)
0.20
0.15
0.10
0.05
0.00
***
ns
G27D
R161W
G27D
R161W
Cytoplasm
Nucleus

Figure 6

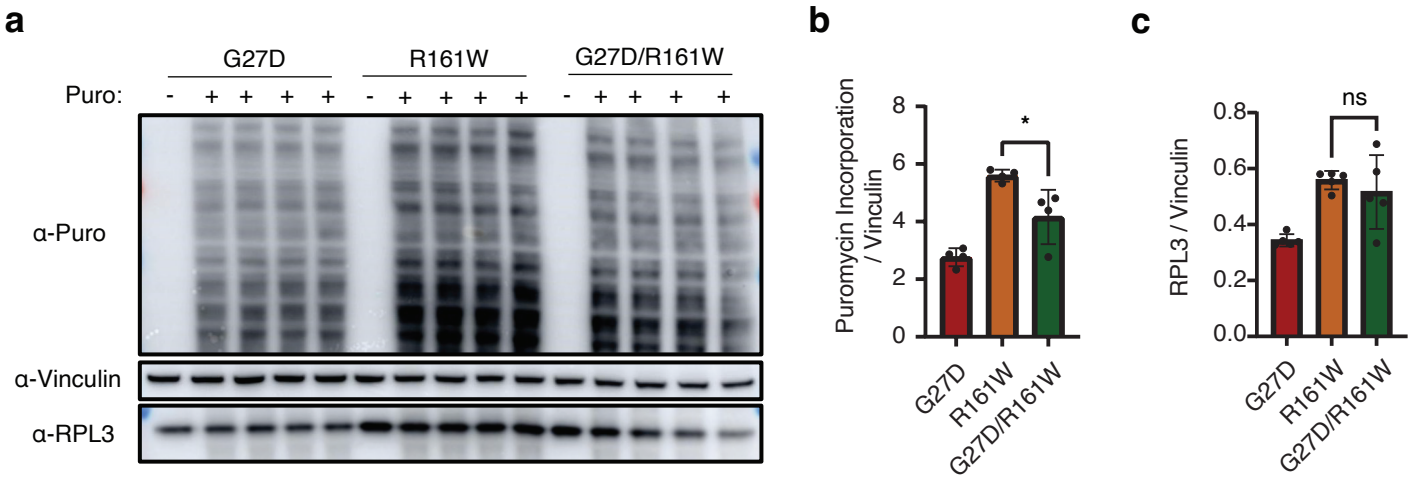
a
G27D
R161W
G27D/R161W
Puro:
- + + + + - + + + + - + + + +
α-Puro
α-Vinculin
α-RPL3
b
Puromycin Incorporation / Vinculin
8
6
4
2
0
*
G27D
R161W
G27D/R161W
c
RPL3 / Vinculin
0.8
0.6
0.4
0.2
0.0
ns
G27D
R161W
G27D/R161W

Extended Data Figure 1

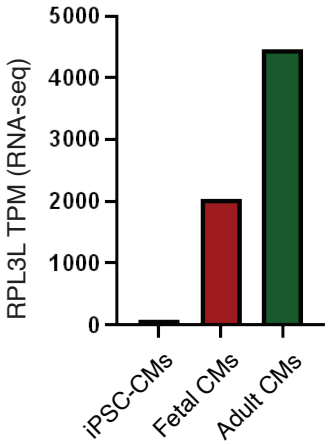

Extended Data Figure 2

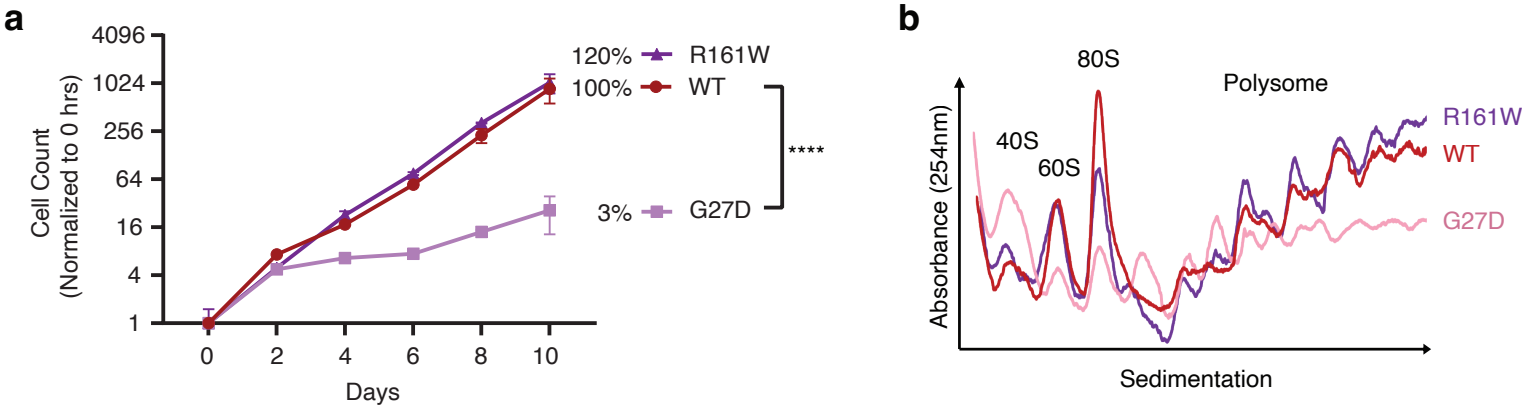

Extended Data Figure 3

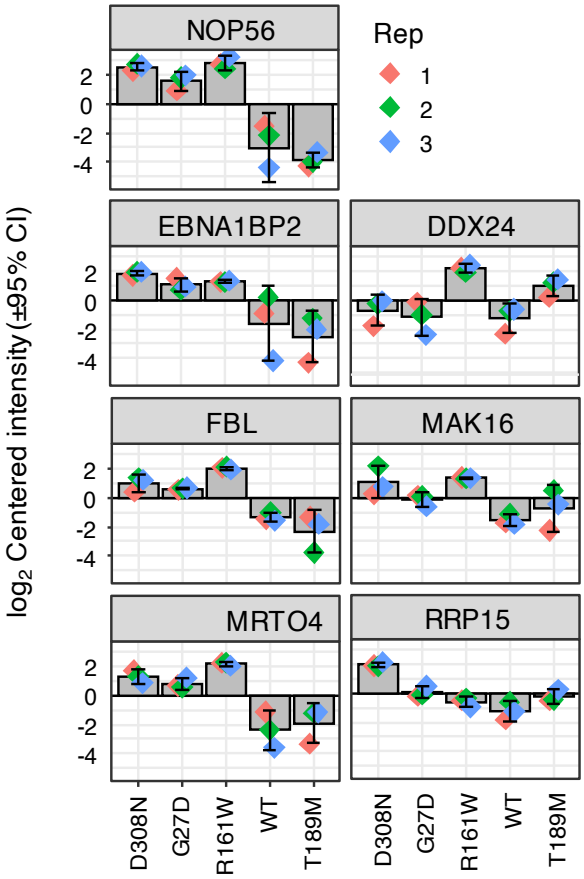

Extended Data Figure 4

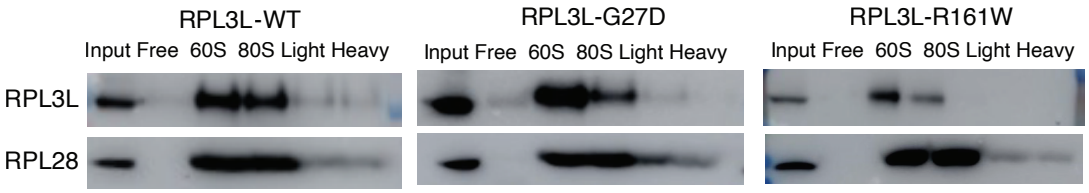

Extended Data Figure 5

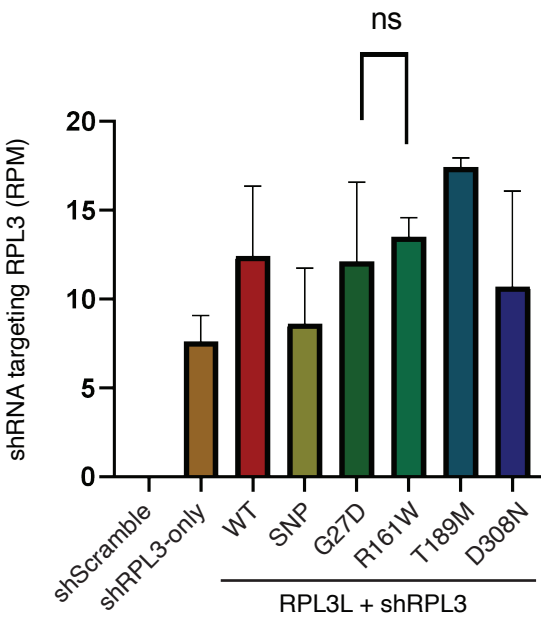
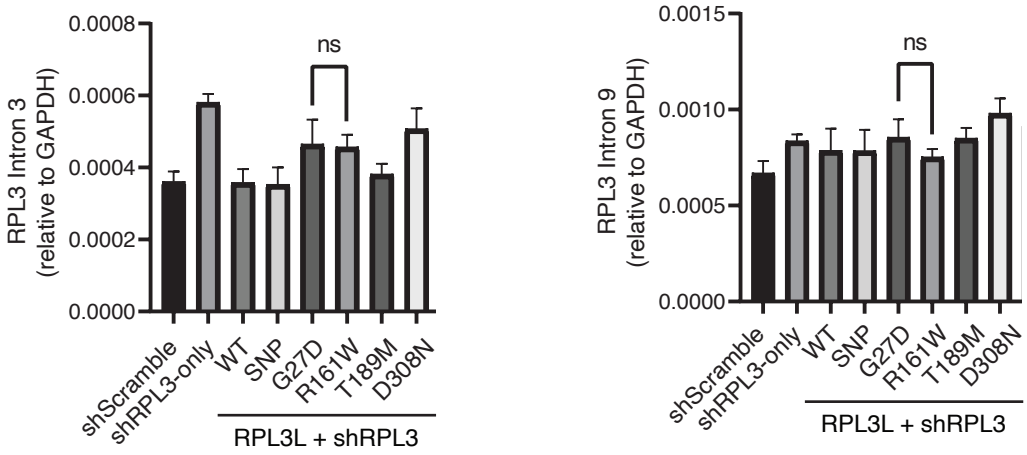
Extended Data Figure 6